Mineralium Deposita (2018) 53:947–966
https://doi.org/10.1007/s00126-017-0777-x

ARTICLE

# A genetic link between magnetite mineralization and diorite intrusion at the El Romeral iron oxide-apatite deposit, northern Chile

Paula A. Rojas[1] · Fernando Barra[2] · Martin Reich[2] · Artur Deditius[3] · Adam Simon[4] · Francisco Uribe[5] · Rurik Romero[2] · Mario Rojo[6]

Received: 31 July 2017 / Accepted: 17 November 2017 / Published online: 5 January 2018


## Abstract

El Romeral is one of the largest iron oxide-apatite (IOA) deposits in the Coastal Cordillera of northern Chile. The Cerro Principal magnetite ore body at El Romeral comprises massive magnetite intergrown with actinolite, with minor apatite, scapolite, and sulfides (pyrite ± chalcopyrite). Several generations of magnetite were identified by using a combination of optical and electron microscopy techniques. The main mineralization event is represented by zoned magnetite grains with inclusion-rich cores and inclusion-poor rims, which form the massive magnetite ore body. This main magnetite stage was followed by two late hydrothermal events that are represented by magnetite veinlets that crosscut the massive ore body and by disseminated magnetite in the andesite host rock and in the Romeral diorite. The sulfur stable isotope signature of the late hydrothermal sulfides indicates a magmatic origin for sulfur ($\delta^{34}S$ between − 0.8 and 2.9‰), in agreement with previous $\delta^{34}S$ data reported for other Chilean IOA and iron oxide-copper-gold deposits. New $^{40}Ar/^{39}Ar$ dating of actinolite associated with the main magnetite ore stage yielded ages of ca. 128 Ma, concordant within error with a U-Pb zircon age for the Romeral diorite (129.0 ± 0.9 Ma; mean square weighted deviation = 1.9, $n = 28$). The late hydrothermal magnetite-biotite mineralization is constrained at ca. 118 Ma by $^{40}Ar/^{39}Ar$ dating of secondary biotite. This potassic alteration is about 10 Ma younger than the main mineralization episode, and it may be related to post-mineralization dikes that crosscut and remobilize Fe from the main magnetite ore body. These data reveal a clear genetic association between magnetite ore formation, sulfide mineralization, and the diorite intrusion at El Romeral (at ~ 129 Ma), followed by a late and more restricted stage of hydrothermal alteration associated with the emplacement of post-ore dikes at ca. 118 Ma. Therefore, this new evidence supports a magmatic-hydrothermal model for the formation of IOA deposits in the Chilean Iron Belt, where the magnetite mineralization was sourced from intermediate magmas during the first Andean stage. In contrast, the beginning of the second Andean stage is characterized by shallow subduction and a compressive regime, which is represented in the district by the emplacement of the Punta de Piedra granite-granodiorite batholith (100 Ma) and marks the end of iron oxide-apatite deposit formation in the area.

**Keywords** Iron oxide-apatite · Sulfur stable isotopes · Geochronology · Northern Chile

Editorial handling: B. Lehmann

**Electronic supplementary material** The online version of this article (https://doi.org/10.1007/s00126-017-0777-x) contains supplementary material, which is available to authorized users.

✉ Paula A. Rojas
paurojas@ing.uchile.cl

[1] Department of Geology, Universidad de Chile, Plaza Ercilla 803, Santiago, Chile

[2] Department of Geology and Andean Geothermal Center of Excellence (CEGA), Universidad de Chile, Plaza Ercilla 803, Santiago, Chile

[3] School of Engineering and Information Technology, Murdoch University, 90 South Street, Murdoch, WA 6150, Australia

[4] Department of Earth and Environmental Sciences, University of Michigan, 1100 North University Ave, Ann Arbor, MI, USA

[5] Servicio Nacional de Geología y Minería (SERNAGEOMIN), Santiago, Chile

[6] Compañia Minera del Pacífico (CAP), Pedro Pablo Muñoz, 675 La Serena, Chile

## Introduction

Iron oxide-apatite (IOA) deposits, also known as magnetite-apatite or Kiruna-type deposits, are a major source of iron and potentially of rare-earth elements (REEs). The genesis of these deposits remains controversial, and both purely magmatic processes and hydrothermal replacement models have been proposed to explain their origin. The magmatic hypothesis proposes that the massive magnetite ore bodies are formed by a Fe-rich immiscible melt that physically separates from its Si-rich conjugate, ascends, and is emplaced with and/or within volcanic sequences (Frutos and Oyarzún 1975; Nyström and Henríquez 1994; Naslund et al. 2002). Hydrothermal replacement models, on the other hand, involve exsolution of Fe-rich magmatic-hydrothermal fluids from dioritic magmas followed by metasomatic replacement/leaching of volcanic (andesite) host rocks (Bookstrom 1977; Parak 1975; Ménard 1995; Rhodes et al. 1999; Sillitoe and Burrows 2002). A more recent model merges these divergent processes into a single sequence of magmatic-hydrothermal events that explains all characteristic features of IOA deposits (Knipping et al. 2015a, b). This model involves the flotation of buoyant, igneous magnetite-fluid bubble aggregates that ascend and segregate within the magmatic chamber in a process analogous to the mineral flotation process used in extractive metallurgy. The growth and accumulation of primary magnetite is followed by precipitation of hydrothermal magnetite from Fe-rich fluids during decompression, resulting in magnetite textures characterized by core-to-rim zonation from igneous to magmatic-hydrothermal. The model proposed by Knipping et al. (2015a, b) involves a genetic and temporal link between magnetite mineralization and diorite magma intrusion. These aspects are investigated here at the El Romeral iron oxide-apatite district in northern Chile, where massive magnetite mineralization is spatially associated with a dioritic intrusion.

The El Romeral iron mine is located 22 km north of La Serena, at the southern edge of the Cretaceous Chilean Iron Belt (CIB), which extends from ca. 26° to 30° lat. S in the Coastal Cordillera of northern Chile (Fig. 1). El Romeral is currently owned by Compañía Minera del Pacífico S.A. (CMP) and is one of the largest IOA districts in Chile with currently estimated resources of 451.1 Mt with 28.2% Fe (CAP Minería 2015 annual report). The deposit was discovered at the beginning of the twentieth century, but production only started during the early 1960s. During the last decade, mining has been intermittent due to variations of Fe ore prices.

Despite its importance, very few studies have been published on El Romeral. Over nearly four decades, pioneering studies by Bookstrom (1975, 1977) are the only published reports that provide a detailed description of the geology of the district and propose a hydrothermal origin for the magnetite ore bodies. In contrast, Alva-Valdivia et al. (2003), based on petrographic and magnetic studies, suggested an origin

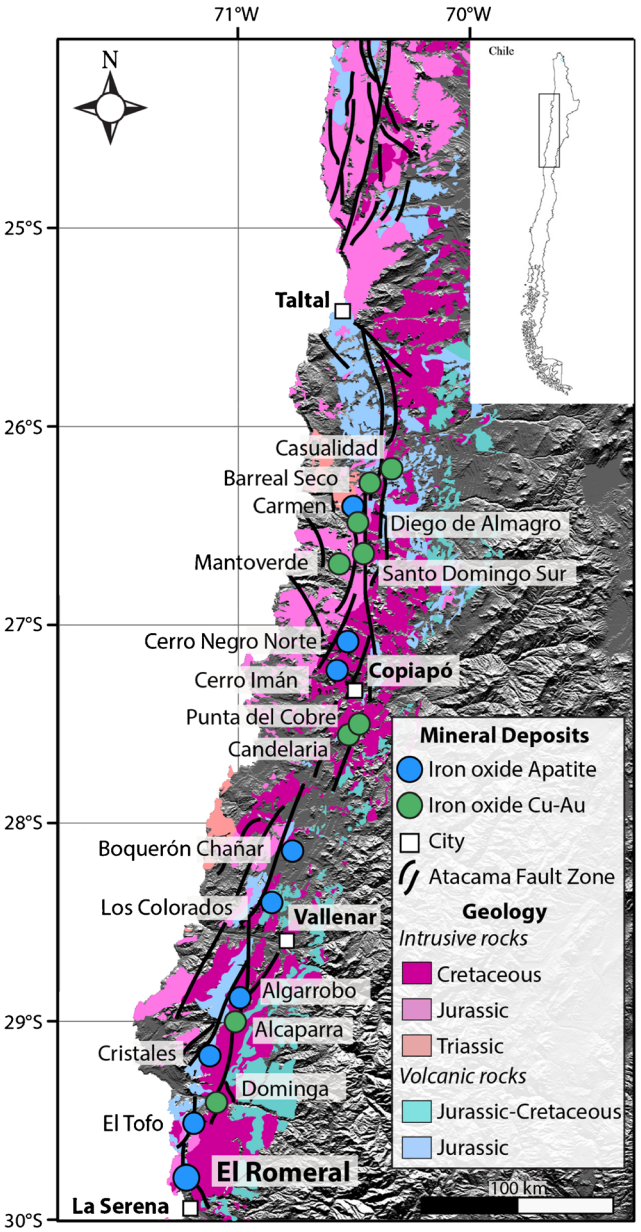


**Fig. 1** Map showing the location of iron oxide-apatite (IOA) and iron oxide-copper-gold (IOCG) deposits in the Cretaceous Chilean Iron Belt, spatially and temporally associated with the Atacama Fault System (modified from Barra et al. 2017)

from iron-rich melts. In this contribution, we provide an update on the geology of the deposit as well as new mineralogical information and sulfur isotope data to better constrain the genesis of the deposit. Most importantly, we present new $^{40}Ar/^{39}Ar$ and U-Pb zircon ages to determine the timing of magnetite ore deposition and its possible relationship with dioritic intrusions. The data reported here, coupled with recent studies at the Los Colorados deposit (Fig. 1) within the same metallogenic belt (Knipping et al. 2015a, b; Bilenker et al. 2016; Reich et al. 2016), provide further constraints on the origin of Cretaceous IOA deposits in northern Chile.

## Geological setting

During Early Jurassic to Early Cretaceous times, the western margin of Gondwana was characterized by an extensional tectonic regime associated with the first Andean tectonic cycle (Coira et al. 1982; Morata and Aguirre 2003). This tectonic setting resulted in the development of two major morphotectonic features: a trench-parallel magmatic arc associated with shear zones, i.e., the Atacama Fault System (AFS), and an eastern back-arc basin (Brown et al. 1993; Scheuber 1994). These features were formed by decoupling of an old and cold oceanic plate with the continental margin (Charrier et al. 2007) during the renewed subduction, caused by the breakup of Gondwana (Jaillard et al. 1990).

The Central Andean iron oxide-copper-gold (IOCG) province of northern Chile and southern Peru formed over a period of ca. 65 Ma (Chen et al. 2013). The initial phase of IOCG mineralization developed during the Middle Jurassic (165–155 Ma), whereas the peak of IOCG-IOA formation occurred during the mid-Cretaceous ca. 130–100 Ma (Oyarzún et al. 2003; Chen et al. 2013). In Peru, IOA and IOCG deposits developed along the axis of the Jurassic-Cretaceous shallow-marine volcanic arc and within the intra-arc Cañete basin (Sillitoe 2003; Chen et al. 2013). Several large deposits have been recognized in the Cañete basin including Raúl-Condestable, Eliana, Monterrosas, Marcona-Mina Justa, Cobrepampa, Pampa de Pongo, and Acarí (Sillitoe 2003; Chen et al. 2010, 2013).

In Chile, several ore deposit types are spatially associated with the AFS. The AFS is a major strike-slip fault system formed during the Late Jurassic and is characterized by an early stage with sinistral polarity (Jurassic to Early Cretaceous), followed by dextral shearing (Late Cretaceous) and final vertical displacements. These displacements were caused by changes in the plate configuration and in the convergence vector of the subducting plate (Scheuber and Andriessen 1990). Mineral deposits associated with this > 1000-km-long fault system include stratabound Cu-(±Ag), porphyry Cu-(Mo), IOCG, and more than 50 world-class IOA deposits, which form part of what is known as the CIB in the Coastal Cordillera of northern Chile (Fig. 1). These ore deposits are mostly hosted in thick mafic-to-intermediate subaerial volcanic units such as La Negra Formation (Middle to Late Jurassic) or Punta del Cobre Formation (Late Jurassic to Early Cretaceous). These units comprise a sequence of basalts, basaltic-andesite, andesite and dacite lavas, tuffs, and lesser sedimentary units that represent the Mesozoic magmatic arc.

Iron oxide-apatite deposits are characterized by the presence of massive magnetite ore bodies with actinolite and minor apatite (usually less than 1% modal), crosscut by late hydrothermal actinolite and sulfide veinlets (mostly pyrite with subordinate chalcopyrite), and diorite to granodiorite dikes (Sillitoe 2003; Barra et al. 2017). The lateral extent of these ore bodies can reach up to several tens of meters, and they are usually discontinuous with massive magnetite grading to a breccia zone with magnetite clasts immersed in an actinolite matrix, followed by an outer low-grade ore zone with magnetite veinlets and disseminated magnetite grains in andesite host rocks that are affected by a pervasive actinolite alteration. In some IOA deposits, such as El Romeral, the ore body is mylonitized in fault zones or shows fluidal textures.

## Deposit geology

El Romeral is hosted by andesite lavas from the La Liga Formation (Late Jurassic to Neocomian), a subunit of the Agua Salada Volcanic Complex (Emparán and Pineda 2005). This formation was intruded at the western margin of the district by diorite intrusions from Late Jurassic to Early Cretaceous (U-Pb zircon age of 145 ± 4 Ma, Emparán and Pineda 2000) and by the Cerro del Cobre batholith (Fig. 2), which comprises Early Cretaceous (U-Pb zircon age of 126.5 ± 2.0 Ma; Emparán and Pineda 2000) monzogranitic to syenogranitic intrusions. The Romeral diorite intruded the andesite host rocks (Figs. 2 and 3) of La Liga Formation and has been considered one of the Late Jurassic-Early Cretaceous diorite intrusions (Emparán and Pineda 2005); however, there are no published ages for these intrusive rocks. Near the Romeral fault, both andesite and the Romeral diorite are affected by pervasive silicification/albitization (Figs. 2 and 4a). The La Liga Formation locally displays minor epidote alteration (Fig. 4b). In the eastern part of the studied area, the post-ore Punta de Piedra granite to granodiorite batholith intruded the andesite sequences (Figs. 2 and 3). These intrusions reflect the Early Jurassic to Late Cretaceous arc migration, which is also evidenced by extrusive units such as the Agua Salada Complex (Early Jurassic-Kimmeridgian), the Arqueros and the overlying Quebrada Marquesa Formations (Kimmeridgian-Tithonian to Albian), and the late Early Cretaceous Quebrada La Totora Beds (Charrier et al. 2007). Additionally, NW to NNW-trending pre-, syn-, and post-ore diorite to granodiorite dikes cut the volcanic host rock (Fig. 2) and the Romeral diorite (Bookstrom 1977). Pre-ore diorite dikes can be either iron-enriched or iron-depleted, suggesting the existence of magmas with different compositions before the formation of the deposit (Bookstrom 1977). Syn-ore dikes display a diorite affinity with accessory Ti-rich magnetite. Post-ore dikes have a more variable composition from diorite to albite, quartz, or K-feldspar-dominant intrusions. Bookstrom (1975) interpreted this compositional range as a strong differentiation after ore formation.

Mineralization at El Romeral is hosted by three main ore bodies: Cerro Principal, Cerro Norte, and Extensión Sur (Espinoza 2000) (Fig. 2). The largest is the Cerro Principal, and it is characterized by a subvertical ore body with massive magnetite and minor actinolite (Figs. 3 and 4c), an outer

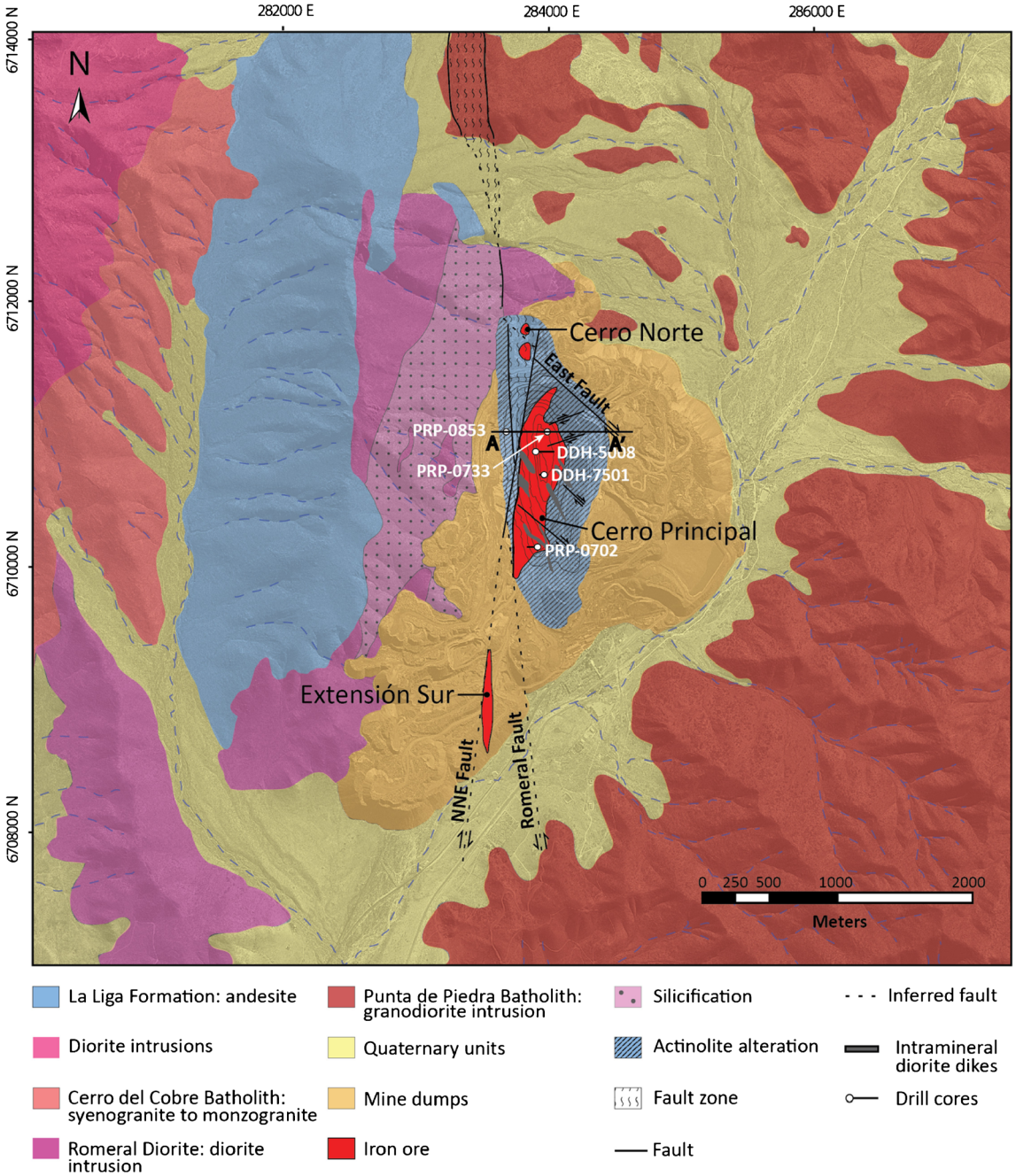


**Fig. 2** Geologic map of the El Romeral district showing major geologic units and the main ore bodies. Also shown is the location of the five drill cores studied here and the position of cross section AA' (modified from the CAP Minería report)

breccia zone with deformed magnetite clasts immersed in an actinolite and scapolite matrix or intergrown with large actinolite crystals (Fig. 4d, e), and an outermost alteration halo with fine-grained actinolite and disseminated magnetite in the andesite host rock. The Cerro Principal massive ore body has an iron grade exceeding 60% Fe, whereas in the breccia zone, the iron grade ranges between 22 and 45%. Additionally, a secondary iron event of magnetite veinlets crosscuts the Cerro Principal magnetite ore body.

Cerro Norte and Extensión Sur are smaller, uneconomic ore bodies located at the outer edge of the current pit (Fig. 2). Cerro Norte comprises the northernmost massive magnetite body and is characterized by low phosphorus and sulfur contents. The ore body is parallel to the Romeral fault and is crosscut by the East fault (Fig. 2). On the southern section of El Romeral, the Extensión Sur mineralization comprises massive and brecciated magnetite with high contents of P (> 0.3%) and S (> 1%).

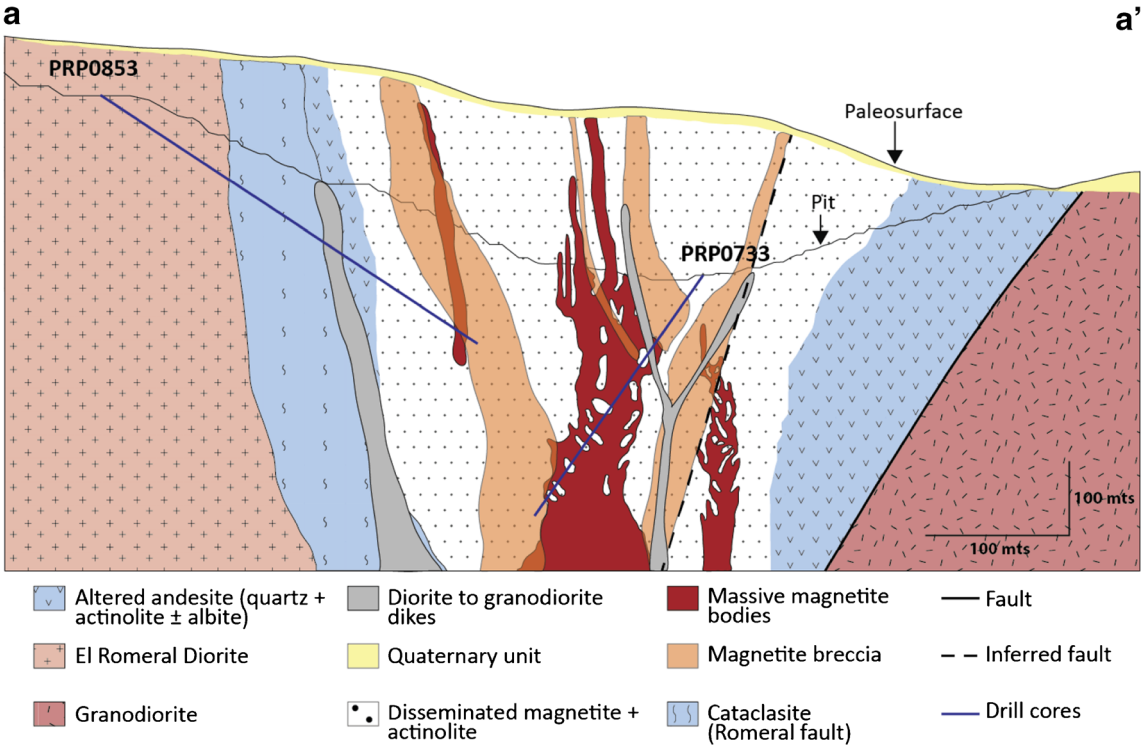


**Fig. 3** Cross-section (AA') of the Cuerpo Principal showing the geometry of the massive magnetite subvertical bodies and the relationship with the host rock

The El Romeral magnetite ore bodies were emplaced along the sinistral NNW strike-slip Romeral Fault System (RFS), which is part of the Romeral-La Silla del Gobernador segment (Charrier et al. 2007), an extension of the Atacama Fault System (Figs. 1 and 2). Brittle and ductile domains are described in fault zones, represented by brecciated areas and by mylonite zones or by foliated host rocks with predominant actinolite crystals oriented along faults, respectively. Previous dating of these fault zones yielded ages between 115 ± 4 and 100 ± 2 Ma (K-Ar ages on biotite and whole rock, and $^{40}Ar/^{39}Ar$ inverse isochron age, Emparán and Pineda 2000, 2005). These ages represent the late basin inversion episode caused by a change from a steep subduction angle to a compressive or low-angle Andean-type subduction (Maksaev 1990; Scheuber and Andriessen 1990).

The Cerro Principal ore body is limited on the western side by the NNE dextral fault and on the eastern side by the East fault (Fig. 2). This post-ore NNW strike-slip fault has a 65°–70° SW dip and records an early sinistral stage followed by a later dextral displacement (Bookstrom 1977). Two additional minor fault systems are recognized in the mine pit, one with a NNW direction similar to the East fault and the other with a NE direction (Fig. 2). Both are dextral systems with magnetite clasts immersed in an actinolite matrix with minor scapolite and apatite.

## Samples and methods

Five drill cores from El Romeral were selected for mapping and sampling: three from the northern section (drill cores PRP-0853, 500 m; PRP-0733, 432.4 m; DDH-5008 436.2 m), one from the central area (DDH-7501, 337.3 m), and one from the southern section (PRP-0702, 400 m) (Fig. 2). Eighty-seven polished thin sections were studied using reflected and transmitted light microscopy in order to characterize the mineralogy of the deposit and to determine the paragenetic sequence. Further mineral identification and characterization were performed by using scanning electron microscopy (SEM) techniques. Additionally, two samples were selected for $^{40}Ar/^{39}Ar$ dating (biotite sample URM-118t; actinolite sample URM-115t) and two samples for U-Pb zircon dating: one from the Romeral diorite and the other from the Punta de Piedra batholith in order to constrain the magmatic history of the district and its connection with Fe mineralization.

### Scanning electron microscopy

SEM observations were performed at the Andean Geothermal Center of Excellence (CEGA), Universidad de Chile in Santiago, using a FEI Quanta 250 SEM equipped with secondary electron (SE), backscattered electron (BSE), cathodoluminescence (CL), and X-ray energy-dispersive spectrometry (EDS) detectors. An acceleration voltage of

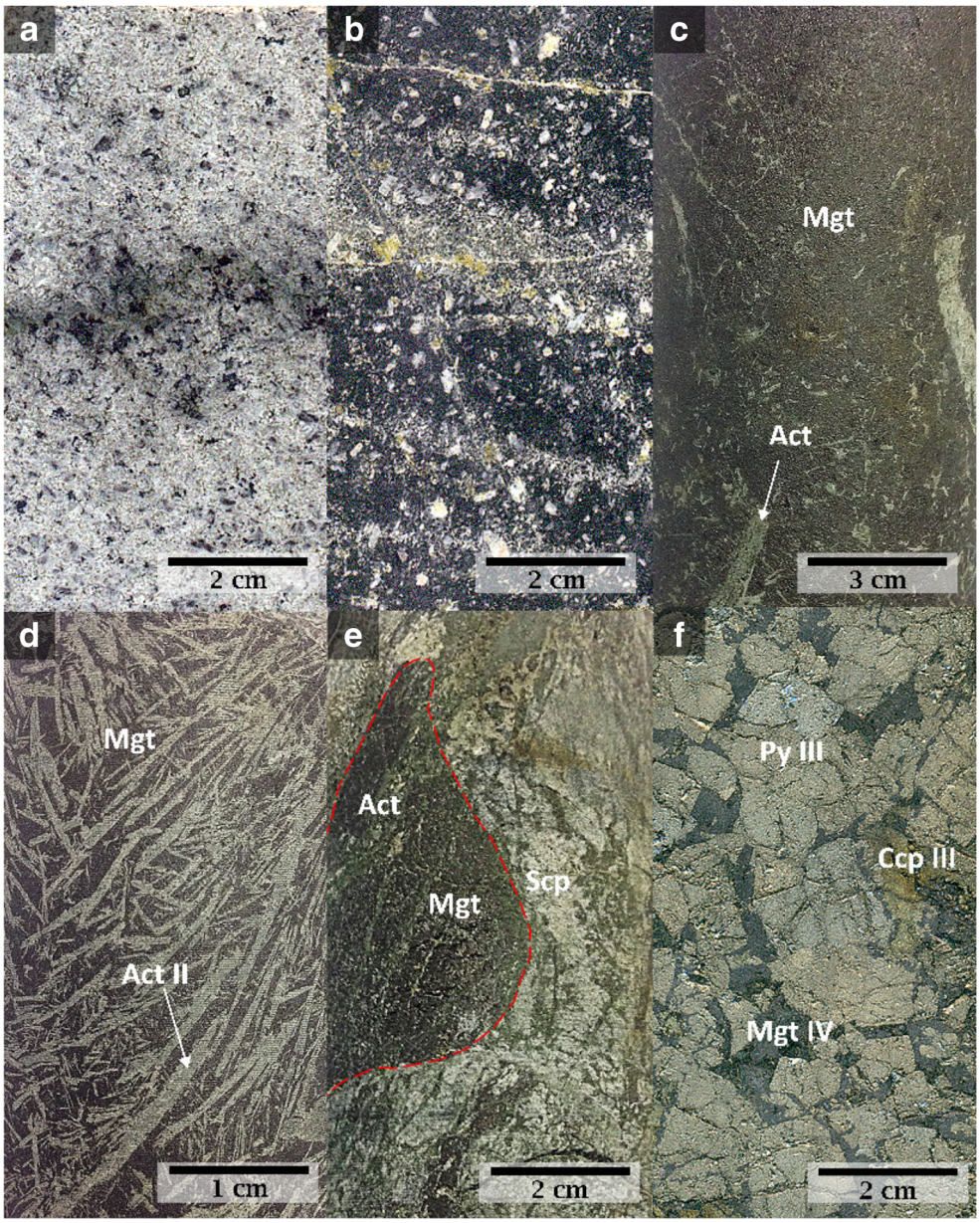


**Fig. 4** Drill-core samples from the different units identified in the El Romeral. **a** Romeral diorite with pervasive silicification. **b** La Liga andesite with minor epidote alteration. **c** Massive magnetite mineralization (magnetite I, magnetite II) with minor actinolite (actinolite I, actinolite II). **d** Actinolite (actinolite II) intergrown with magnetite (magnetite I, magnetite II). **e** Fault zones with mylonite magnetite clasts (magnetite I, magnetite II) immersed in a scapolite and actinolite (actinolite II) matrix. **f** Sulfide (pyrite III and chalcopyrite III) breccia clasts in a magnetite matrix (magnetite IV). Mgt magnetite, Act actinolite, Scp scapolite, Py pyrite, Ccp chalcopyrite. See text for discussion

20 kV and a beam current of 80 μA were used. Semi-quantitative analyses were carried out on selected minerals to confirm petrographic identification and on scapolite crystals in order to discriminate between the different end members of the group, i.e., meionite, marialite, or the (Ca, Na) solid solution silvialite. The INCA software was used for measurements and data processing.

## $^{40}Ar/^{39}Ar$ dating

Two samples were selected for $^{40}Ar/^{39}Ar$ dating from drill core DDH-5008 (283537E/6708604N). Sample UMR-115t (93 m a.s.l.) comprises massive magnetite intergrown with centimeter-sized actinolite crystals. Sample URM-118t (291 m a.s.l) corresponds to the Romeral diorite and contains disseminated magnetite associated with secondary biotite. Both samples were first studied under a petrographic microscope in order to select unaltered minerals. Several actinolite grains were handpicked from the crushed sample and split into two subsamples, and about ten biotite crystals were selected for analysis. The actinolite and biotite samples, as well as Fish Canyon standard and Ca and K salts, were irradiated at the Nuclear Research Center of La Reina, Santiago, Chile, and later stored for 3 months in order to decrease sample activity. The $^{40}Ar/^{39}Ar$ measurements were performed at the SERNAGEOMIN Argon-Argon Laboratory in Santiago, Chile, by using a Mass Analyzer Products (MAP) model 215-50 mass spectrometer with an electron multiplier

(Johnston MM1-1SG), integrated $CO_2$ laser, gas extraction system (Merchantek MIR10-TP), and automated line composed of one SAES ST-101 Zr-Al getter (450 °C) and two SAES ST-172 Zr-V-Fe getters. Analyses of Ca and K salts were used for correction of isotope interferences, and the Fish Canyon standard was used for determination of the J-factor. Data were reduced using the ArArCALC v2.4 software (Koppers 2002).

### U-Pb zircon dating

Two samples from intrusive rocks were selected for U-Pb zircon dating in order to constrain the magmatic history in the El Romeral district. Sample Rom-Gd was collected from the Punta de Piedra granodiorite batholith, from an outcrop located on the east side of the pit (284000E/6708000N; 161 m a.s.l.), and sample ROM-109 from the Romeral diorite, at the west margin of the main ore body (283480E/6711016N; 350 m a.s.l.). Sample preparation and analyses were performed at the Sample Preparation Laboratory and at the CEGA Isotope Geochemistry Lab at the Universidad de Chile. Rock grinding was carried out by using first a jaw crusher followed by a disc mill. Samples were sieved, and the fraction smaller than 500 μm was collected. Heavy mineral fractions were concentrated using a Gemini water table, followed by a Frantz isodynamic magnetic separator. Subsequently, zircons were separated by using heavy liquids (tetrabromomethane and/or methylene iodide decantation) and final handpicking under a binocular microscope. Approximately 50 zircon grains per sample were mounted in epoxy resin with Plešovice (Sláma et al. 2008) and Temora2 (Black et al. 2004) standards. The sample-standard mount was polished before analysis, and CL images of zircon crystals were obtained by using a FEI Quanta 250 SEM coupled with a Centaurus sensor. These images were used to assess zoning and inherited components. Uranium-Pb dating was performed by laser ablation multicollector inductively coupled plasma mass spectrometry (LA MC-ICPMS). Analyses were conducted on 30-μm-diameter spots using an Analyte G2 ArF excimer laser ablation system with a 193 nm wavelength. Ablated material was transported by a helium flux with a rate of 0.5 LPM into a Neptune Plus MC-ICPMS. Measurements were performed using the sample-bracketing method, and data reduction and plots were carried out with Iolite (Paton et al. 2011) and Isoplot 4.0 (Ludwig 2010), respectively.

### Stable isotopes of sulfur

Eight sulfide samples were collected for sulfur isotope analysis: five from drill core PRP-0702, two from PRP-0853, and one from DDH-5008 (Fig. 2). Style of mineralization and depth were main criteria for sample selection. Samples ROM-017 (79.50 m), ROM-018 (84.65 m), and ROM-023 (133.95 m) consist of minor magnetite and quartz in pyrite veinlets. Samples ROM-019 (87.40 m) and ROM-020 (89.95 m) were collected from magnetite breccias with euhedral pyrite clasts (Fig. 4f). Samples ROM-125 (215.85 m), ROM-139 (410.1 m), and ROM-177 (410.13 m) were collected from the cataclastic zone and include magnetite and pyrite, with minor quantities of actinolite, chalcopyrite, and apatite; sample ROM-177 (410.75 m) is an actinolite veinlet with pyrite. All analyzed sulfide samples represent the main sulfide event (event II) with pyrite III and/or chalcopyrite III. Mineral concentrates with > 99% pure pyrite were obtained by crushing followed by handpicking under a binocular Olympus microscope. Mineral concentrates were analyzed at the Environmental Isotope Laboratory, Department of Geosciences, University of Arizona, Tucson. A continuous-flow isotope-ratio mass spectrometer (CF-IRMS) ThermoQuest Finnigan Delta PlusXL model coupled with a Costech elemental analyzer was used for sulfur isotope ratio measurements. Before analyzing samples, concentrates were introduced into a combustion chamber with $O_2$ and $V_2O_5$ (Coleman and Moore 1978) obtaining an $SO_2$ gas at 1030 °C, which is the analyzed product. The system was calibrated by using two international standards: OGS-1, which is $BaSO_4$, precipitated from seawater, and NBS123, a sphalerite sample with a $\delta^{34}S$ reported value of + 17.09‰ (NIST reference materials, https://www.nist.gov). A linear calibration between − 10 and + 30‰ was performed, and a precision of ± 0.15 or 1$\sigma$ was estimated by diverse internal standard measurements (http://www.geo.arizona.edu/node/153). Sulfur isotope data are reported in delta notation, where $\delta^{34}S = [[(^{34}S/^{32}S)_{sample} - (^{34}S/^{32}S)_{standard})] / (^{34}S/^{32}S)_{standard}] \times 1000‰$.

## Results

### Iron ore mineralogy

Mineralization at El Romeral comprises three ore bodies: Cerro Principal, Cerro Norte, and Extensión Sur. Cerro Norte and Extensión Sur are located at the outer northern and southern edges of the pit, respectively (Fig. 2). Production was developed around the Cerro Principal ore body, which consists of subvertical massive magnetite (Figs. 3 and 4c) intergrown with large actinolite crystals (Figs. 4d and 5a). Massive magnetite grades outward to a breccia or mylonite near fault zones (Fig. 4e) and disseminated magnetite with actinolite and minor sulfides. Several granite to diorite dikes cut the main ore body, and some of them are mineralized (Bookstrom 1977).

Three types of magnetite grains have been identified in the massive magnetite ore body: an inclusion-rich magnetite (magnetite I, Fig. 5b) mainly with quartz (I), oxide (ilmenite,

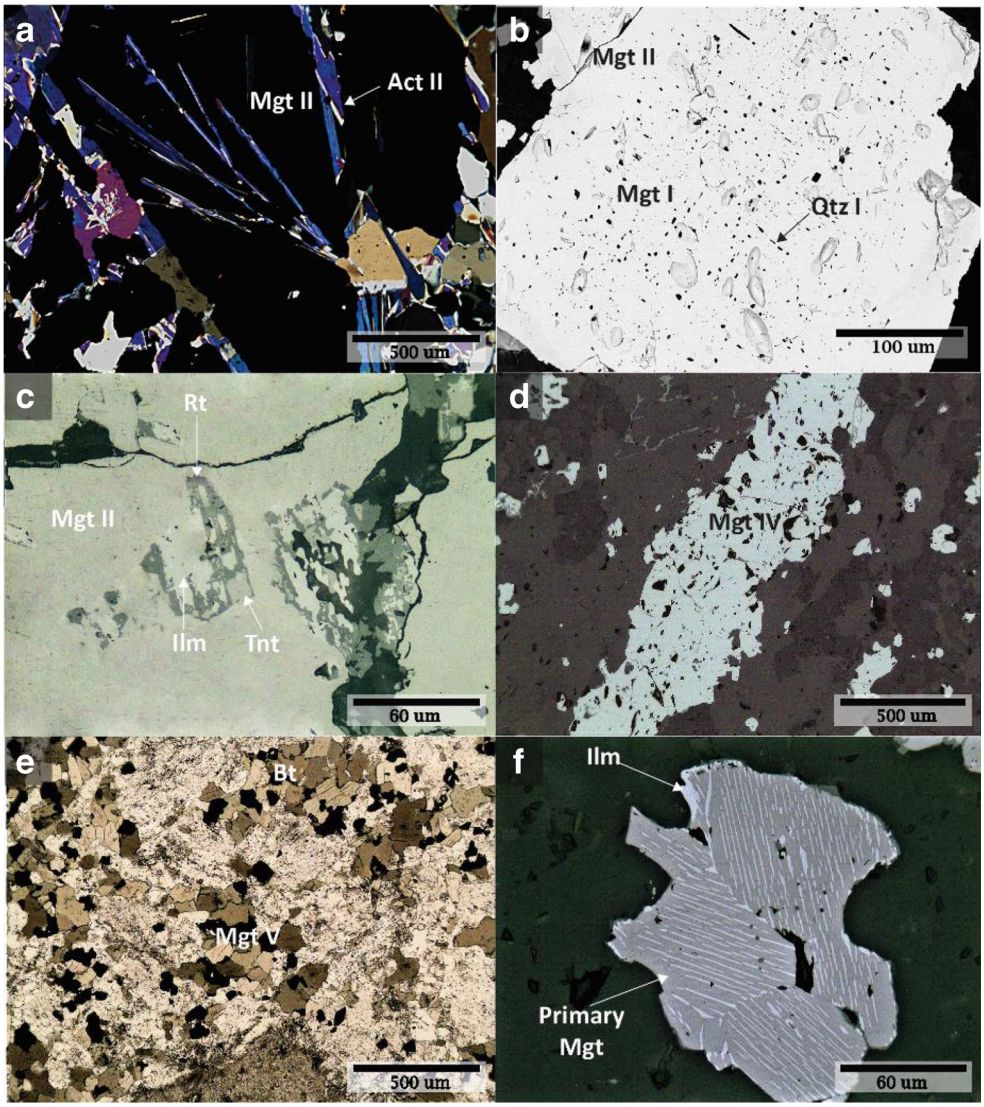


**Fig. 5** Photomicrographs (**a**, **c**–**f**) and backscattered electron image (**b**) of the magnetite ore event. **a** Actinolite II intergrown with magnetite II from the massive ore bodies (transmitted light, CPL). **b** Two major magnetite types: inclusion-rich magnetite I, with euhedral quartz I oriented inclusions, and inclusion-poor magnetite II. **c** *Patches* of ilmenite and titanite, surrounded by rutile, contained in magnetite II crystals (reflected light, PPL). **d** Magnetite IV veinlets crosscutting the andesite host rocks. **e** Secondary biotite with magnetite type V (transmitted light, PPL). **f** Primary magnetite with ilmenite exsolution lamellae (reflected light, PPL). Mgt magnetite, Act actinolite, Qtz quartz, Py pyrite, Ilm ilmenite, Tnt titanite, Bt biotite

rutile) and minor sulfide (pyrite I ± chalcopyrite I) inclusions, and an inclusion-poor magnetite (magnetite II). A chemically zoned magnetite (magnetite III) has also been recognized at shallow levels in the deposit; however, its distribution is restricted to outermost zones from the massive ore body at depths < 100 m. Magnetite I was observed to be surrounded by magnetite II. Ilmenite, rutile, and titanite *patches* are present in magnetite II grains (Fig. 5c). Additionally, an assemblage of actinolite I, quartz II, and clinopyroxene was observed in the interstices between magnetite II crystals. This interstitial space can sometimes contain sulfides (pyrite II, chalcopyrite II). A fourth type of magnetite (magnetite IV) is observed as thin veinlets that crosscut the massive ore body (Fig. 5d). A final spatially restricted event of magnetite mineralization (magnetite V) is observed as fine grains of magnetite associated with secondary biotite (Fig. 5e) in the andesite host rock and in the Romeral diorite. Finally, disseminated primary magnetite grains with ilmenite exsolution lamellae (Fig. 5f) were identified in the andesite from La Liga Formation. Description of each type of magnetite is shown in Table 1.

## Gangue mineralogy

The dominant hydrothermal alteration types in El Romeral include silicification with minor albite and abundant actinolite. The former is observed as a widespread pre-ore and pervasive event (Figs. 4a and 6a) that affected the andesite host rock and the Romeral diorite, proximal to the Romeral fault zone, at the western margin of the deposit (Fig. 2). This alteration was previously described as aplitization that affected the actinolitized Romeral diorite after ore deposition (Bookstrom 1977). This author described six subzones with variable amounts of quartz, plagioclase, and minor microcline. However, this alteration is described here as pre-ore alteration, where quartz is the dominant phase, along with subordinate

**Table 1** Magnetite types observed in the El Romeral district

| Magnetite type | Main features |
|---|---|
| Type I | Inclusion-rich magnetite with chalcopyrite, pyrite, oxides (ilmenite and rutile), and euhedral quartz inclusions, oriented along crystallographic planes |
| Type II | Inclusion-poor magnetite<br>Associated to actinolite I, quartz II, pyroxene, and sulfides (pyrite and chalcopyrite) which are trapped between magnetite crystals<br>At the edges of massive magnetite ore bodies, it is in association with centimeter-sized actinolite (II) |
| Type III | Inclusion-poor, chemically zoned magnetite<br>At local shallow zones from the massive ore bodies (< 100 m) |
| Type IV | Thin magnetite veinlets (< 0.5 cm) that crosscut the massive magnetite ore bodies |
| Type V | Magnetite and biotite aggregates, displayed as disseminated mineralization in the host rocks |

albite, and where oligoclase is found only as a primary and accessory mineral of the diorite intrusion. No microcline was observed in the studied samples. Actinolite is modally dominant over quartz near the massive magnetite ore body. Two forms of actinolite were identified: small (< 500 μm) actinolite crystals (actinolite I) with quartz (quartz II) and clinopyroxene within magnetite II crystals (Fig. 6b) and a second type that corresponds to a later syn-ore crystallization of acicular to tabular, centimeter-sized actinolite (actinolite II) grains (Fig. 5a). Actinolite II is usually observed at shallow levels and/or at the margins of the magnetite ore body, and as an alteration halo due to the crystallization of the massive magnetite. Actinolite II has a fibrous to acicular habit and shows a preferred orientation in fault zones (Fig. 6c). Primary hornblende crystals from the andesite host rock also display reaction rims with actinolite, followed by chlorite replacement.

A late actinolite event (actinolite III) is present as the matrix of magnetite breccias near fault zones and thin veinlets related to sulfide mineralization, i.e., pyrite (pyrite III) with drop-shaped chalcopyrite (chalcopyrite III; Fig. 6d) and pyrrhotite inclusions (Fig. 6e). Chalcopyrite mineralization remains in equilibrium at low-temperature conditions with disseminated chlorite and with chlorite veinlets. This hydrothermal event (Fig. 7) is also associated with Ca-rich fluids, where epidote aggregates, calcite, and disseminated titanite were formed. Titanite was observed as euhedral diamond-shaped crystals, disseminated in the host rock or as anhedral crystals surrounding disseminated magnetite or ilmenite crystals.

Local massive cumulates of scapolite (< 1% modal) and disseminated crystals or veinlets of apatite (< 1% modal) were also observed as part of this hydrothermal event and crosscut by sulfide veinlets (Fig. 7). The chemical composition of scapolite was semi-quantitatively determined using SEM-EDS, with a predominance of Na over Ca within the Na-Ca-Cl-scapolite solid solution.

Finally, hematite replaced magnetite (pseudomorphic replacement) at shallow levels (< 100 m) in the deposit, which most likely resulted from weathering/supergene processes. This event was also responsible for a minor, local copper enrichment with chalcopyrite-bornite replaced by digenite and covellite (Fig. 6f). The paragenetic sequence related to the formation of iron ore bodies (pre-ore events are not shown) is presented in Fig. 7.

## Actinolite $^{40}Ar/^{39}Ar$ ages

In this study, two aliquots of an actinolite II sample (sample URM-115t) were analyzed using a MAP 215-50 mass spectrometer (ESM Table 1, Fig. 8). Both analyses (subsample URM-115t-01 and subsample URM-115t-02) yielded consistent plateau ages with 100% of the Ar gas released. Subsample URM-115t-01 has a plateau age of 127.7 ± 1.5 Ma ($2\sigma$) with a constant Ca/K and Cl/K ratio, excluding the first and second steps for Ca and only the first step for Cl. Higher $^{36}Ar_{(Ca)}$ contributions in steps 4, 6, and 7 are observed with 13, 14, and 37% of $^{36}Ar$, respectively (ESM Table 1), which resulted in a relevant Ca correction. The plateau age is identical within error to the calculated inverse isochron age of 127.8 ± 1.8 Ma ($2\sigma$), and the isochron intercept is consistent with the $^{40}Ar/^{36}Ar$ atmospheric ratio (295.2 ± 3.7). Subsample URM-115t-02 yielded a plateau age of 126.5 ± 2.0 Ma, which is concordant with the previous subsample. Constant Ca/K and Cl/K ratios were obtained, excluding the first, second, third, and final steps for Ca and only the first step for Cl (ESM Table 1). Relevant Ca correction was performed for the first step where a higher $^{36}Ar_{(Ca)}$ contribution is observed (ESM Table 1). The calculated age using the inverse isochron method (126.3 ± 2.1 Ma; $2\sigma$) is consistent with the plateau age, and the isochron intercept indicates an atmospheric contribution for the $^{40}Ar/^{36}Ar$ ratio (295.9 ± 3.0).

## Hydrothermal biotite $^{40}Ar/^{39}Ar$ age

The stepwise heating technique was performed in eight steps at a power range between 3 and 30 W. Six consecutive steps comprise 95.3% of the released gas and yielded an age of

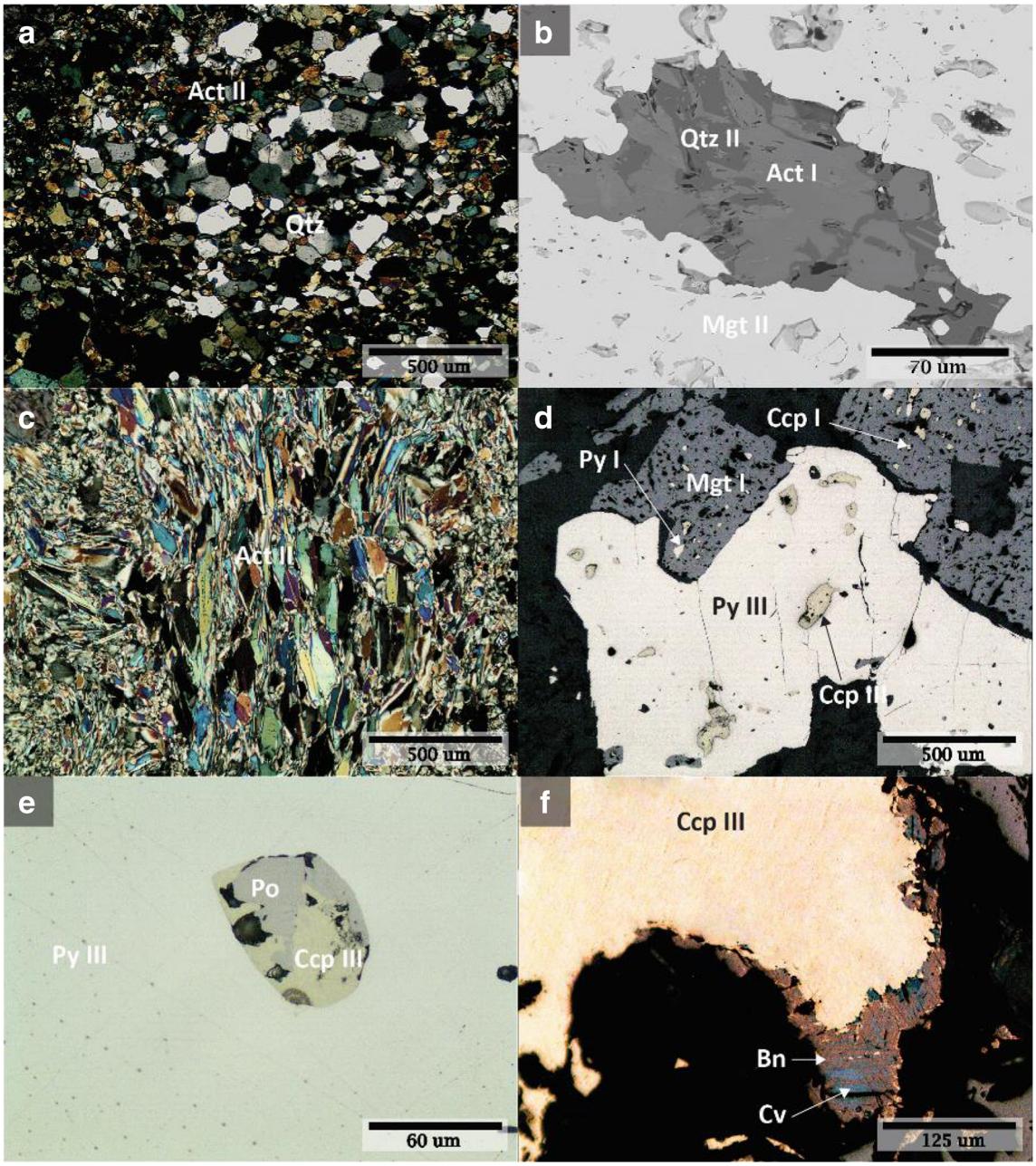


**Fig. 6** Photomicrographs (**a**, **c**–**f**) and backscattered electron image (**b**) of gangue and sulfide mineralization. **a** Pervasive silicification of the andesite host rock (transmitted light, CPL). **b** Syn-ore actinolite I with quartz II, both included in massive magnetite mineralization (magnetite II). **c** Oriented actinolite II crystals located at fault zones (transmitted light, CPL). **d** Two events of sulfide mineralization: (i) pyrite I and chalcopyrite I contained in magnetite I and (ii) inclusions of chalcopyrite III in pyrite III, surrounding magnetite I grains (reflected light, PPL). **e** Chalcopyrite III and pyrrhotite composite inclusion in pyrite III (reflected light). **f** Chalcopyrite III with bornite and later covellite rims (reflected light, PPL). Qtz quartz, Act actinolite, Mgt magnetite, Py pyrite, Ccp chalcopyrite, Po pyrrhotite, Bn bornite, Cv covellite

118.3 ± 0.2 Ma (Fig. 9). The $^{36}Ar$ contribution produced by Ca decay is negligible, demonstrating a low interference signal. The age determined by using the inverse isochron approach (118.5 ± 0.2 Ma) is consistent with the plateau age. The initial 267.3 ± 2.9 ratio is significantly different to the atmospheric ratio, possibly because most data points plot in a cluster at low $^{36}Ar/^{40}Ar$ ratios resulting in a high uncertainty in the upper intercept (Fig. 9). Results are reported in ESM Table 2.

## Zircon U-Pb ages

Zircon grains extracted from the Romeral diorite are prismatic, semi-transparent, colorless crystals, with a

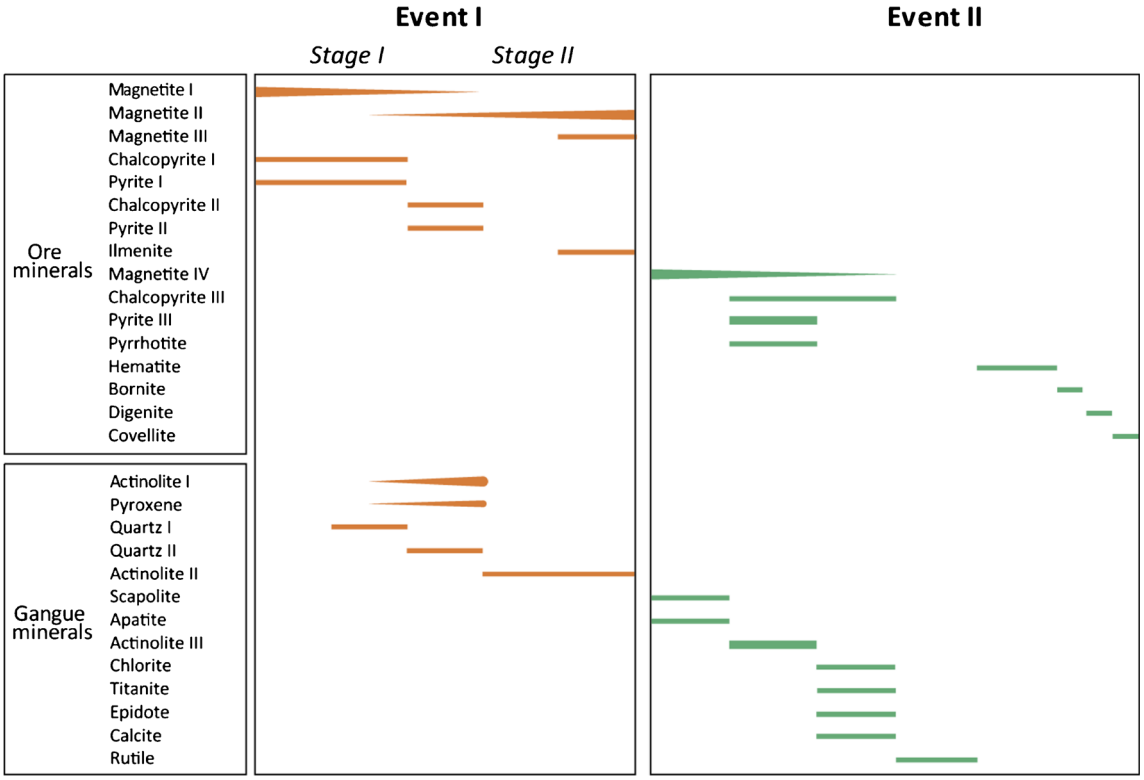


**Fig. 7** Paragenetic sequence showing the two defined events: (i) a first event of massive magnetite ore formation with actinolite, quartz, pyroxene, and minor sulfides and (ii) a second event characterized by magnetite and sulfides in veinlets associated with a calcic alteration. See text for discussion

maximum length of 200 μm. In general, besides the typical igneous oscillatory zoning, zircons display local recrystallization zones, suggesting late-magmatic processes where impurities from unstable trace element-rich zones are expelled and then concentrated in trace element-rich convolute zones, generating a homogeneous zircon domain (Corfu et al. 2003). In order to avoid inaccurate results, these areas of zircon grains were not analyzed. Zircons extracted from the Punta de Piedra sample are clear, prismatic, and colorless and reach up to 300 μm in length. The analyzed zircons show typical oscillatory zoning under SEM-CL observation.

Zircon U-Pb ages are presented in ESM Tables 3 and 4, and Concordia, Tera-Wasserburg, and weighted average age plots are shown in Figs. 10 and 11 for the Romeral diorite and the Punta de Piedra batholith, respectively. The Romeral diorite sample yielded a weighted average age of 129.0 ± 0.9 Ma (mean square weighted deviation (MSWD) = 1.9, $n = 28$) (Fig. 10). Calculated Th/U ratios range from 0.4 to 1.3, indicating a magmatic origin for the zircons. The Concordia and Tera-Wasserburg plots show that the analyses are concordant. For the Punta de Piedra batholith (Fig. 2), a weighted average age of 102.2 ± 2.0 Ma (MSWD = 5.3, $n = 12$) was obtained (Fig. 11). The Th/U ratios of the zircon grains range between 0.5 and 1.5, which is in agreement with Th/U ratios for typical igneous zircons.

### Sulfur isotope data

Sulfur stable isotope data of sulfides, described as part of a hydrothermal mineralization event (event II, Fig. 7), are listed in ESM Table 5. Delta-$^{34}$S values for seven pyrite samples range from − 0.8 to 1.4‰ with a mean of 0.8‰ and a median of 0.5‰. A pyrite ± chalcopyrite (~ 30% chalcopyrite) concentrate (sample ROM-139) shows a heavier sulfur isotopic composition, with a $\delta^{34}$S value of 2.9‰. On the other hand, the two breccia samples (samples ROM-019 and ROM-020) show a consistent $\delta^{34}$S value of 0.5‰, in contrast with a more widespread $\delta^{34}$S range for veinlets, with values between − 0.3 and 1.4‰. A large range of $\delta^{34}$S values is also observed in mylonite samples (samples ROM-125 and ROM-139), where two measurements of − 0.8 and 2.9‰ were obtained (ESM Table 5). Finally, it is noteworthy that no correlation is observed between the depth from which sulfides were sampled in the deposit and $\delta^{34}$S values.

## Discussion

### Ore-forming processes and paragenetic sequence

The El Romeral ore comprises massive, brecciated, and disseminated magnetite with actinolite and minor sulfides. Five types of magnetite are identified (Figs. 5 and 6): (i) a massive, inclusion-rich magnetite I with euhedral quartz I

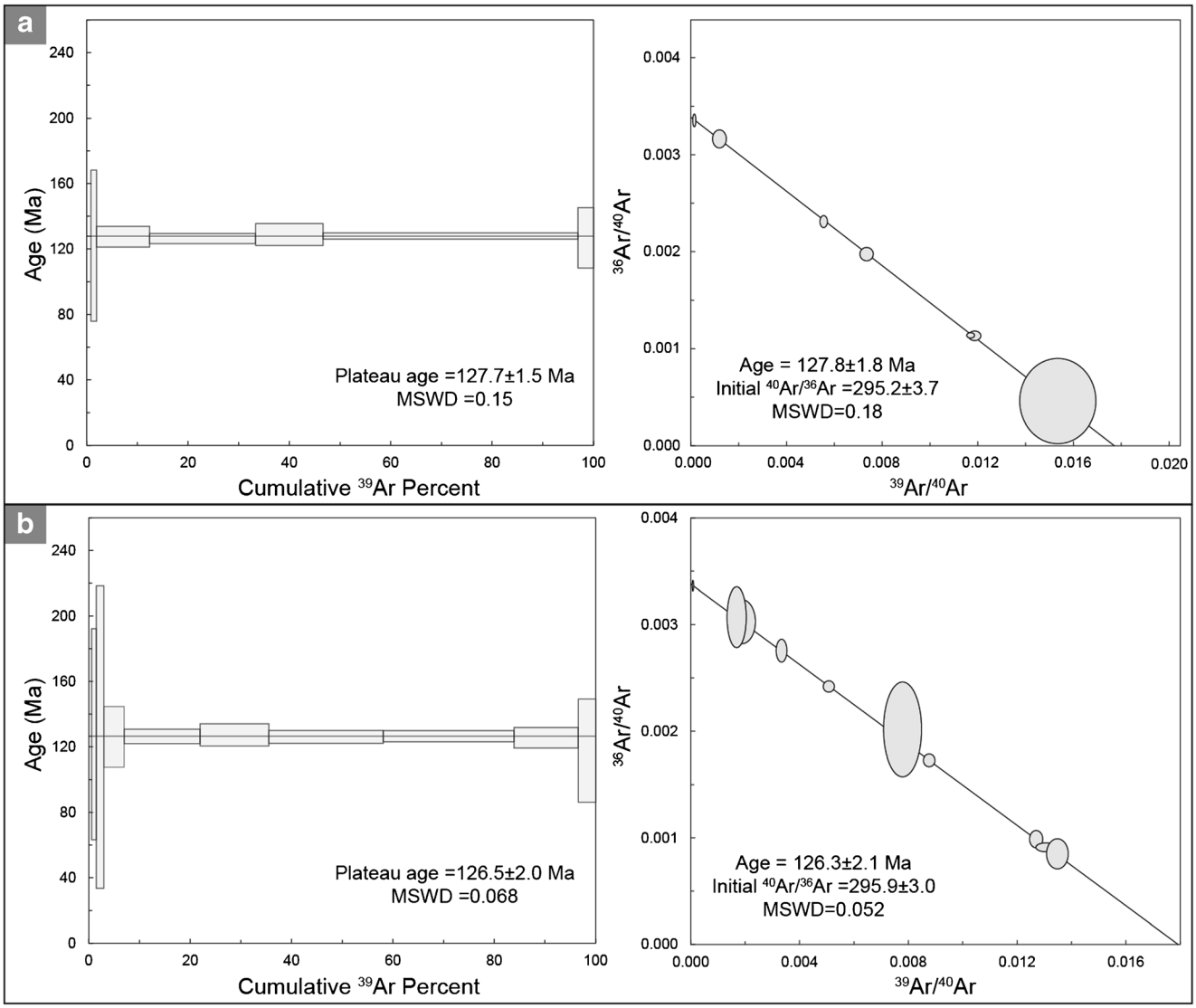


**Fig. 8** $^{40}Ar/^{39}Ar$ dating of subsample URM-115t with uncertainties plotted as $2\sigma$. **a** Plateau age and isochron age of run 01. **b** Plateau age and isochron age of run 02

inclusions (Fig. 5b) and minor chalcopyrite I and pyrite I; (ii) inclusion-poor magnetite II with actinolite I, quartz II (Fig. 6b), clinopyroxene, and minor chalcopyrite II and pyrite II within interstitial spaces of subhedral magnetite crystals (magnetite II is also related to large actinolite II crystals present at the margins of the ore body; Fig. 5a); (iii) a zoned magnetite; (iv) late magnetite veins (magnetite IV; Fig. 5d), in some areas with sulfides or crosscut by apatite veinlets (sulfide mineralization is also related to this vein event, with abundant pyrite III, subordinate chalcopyrite III, and pyrrhotite associated with chlorite); and (v) disseminated magnetite V with hydrothermal biotite (Fig. 5e). The first two magnetite types (i and ii) comprise the main mineralization event (event I, Fig. 7), whereas magnetite III is poorly represented. Magnetite IV and magnetite V are related to two distinct late hydrothermal episodes (event II, Fig. 7).

**Event I** During the first, modally dominant mineralization event, inclusion-rich magnetite cores crystallized. Magnetite I contains chalcopyrite, pyrite, and euhedral quartz inclusions (Fig. 5b). The latter are aligned along crystallographic planes in the magnetite grain, suggesting an exsolution process at a low cooling rate probably related to a magmatic event (Rojas 2017). Chalcopyrite is stable below 557 °C (Pankratz and King 1970) and pyrite below 770 °C at 100 MPa (Kullerud and Yoder 1959). Hence, these sulfides are not stable at igneous conditions, i.e., at temperatures ranging from 800 to 1000 °C (diorite crystallization temperature). Thus, decomposition of a primary (magmatic) intermediate solid solution (ISS) (Jugo et al. 1999) or a slightly S-deficient ISS, $CuFeS_{2-x}$, (Vaughan and Craig 1978) can explain the presence of chalcopyrite inclusions. Pyrite inclusions, on the other hand, could have formed from pyrrhotite or a monosulfide solid solution (Edmonds and Mather 2017).

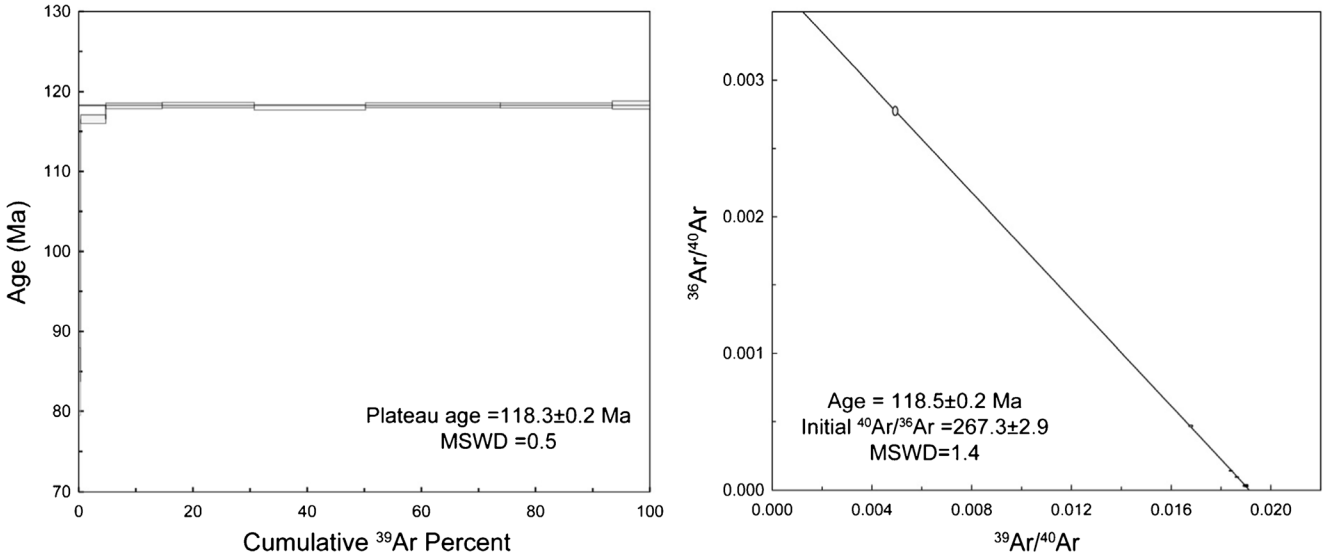


**Fig. 9** $^{40}Ar/^{39}Ar$ ages for hydrothermal biotite with uncertainties at the 2$\sigma$ level

Magnetite II is characterized by its association with actinolite I, quartz II, and pyroxene, all of which are present within magnetite crystals (Fig. 6b). This assemblage could represent accessory microlites incorporated during bubble flotation and/or the chemical composition of the bubble and, therefore, of the magmatic hypersaline fluid. In addition, at the margins of the massive magnetite ore body, large actinolite (actinolite II) crystals with minor sulfides, mainly pyrite with subordinate chalcopyrite, are present in interstitial spaces between euhedral magnetite II crystals. These sulfides are possibly precipitated from fluid-rich bubbles following the model proposed by Knipping et al. (2015a, b).

The textures of magnetite types I and II and the nature of their inclusions are similar to those described by Knipping et al. (2015a) for the Los Colorados IOA deposit, and hence, a combined magmatic/magmatic-hydrothermal origin is a plausible model to explain the origin of the ore mineralization at El Romeral. Ilmenite exsolution lamellae (Fig. 5f) or ilmenite patches in grain rims (Fig. 5c) were identified in primary magnetite crystals from the volcanic host rocks and in magnetite II grains, respectively. The presence of ilmenite patches within magnetite grains is considered as a low-temperature and slow diffusion rate migration, with ilmenite or Ti remaining inside the crystal in which an increase in oxygen fugacity and diffusion will lead to the formation of Ti-rich granules or patches at the rims of a Ti-poor magnetite (Buddington and Lindsley 1964). In contrast, bleb-type ilmenite crystals are formed by high-temperature migration or *granule oxyexsolution* associated with a loss of components from the magnetite structure (Buddington and Lindsley 1964). These textures were previously described at El Romeral by Alva-Valdivia et al. (2003), who explain the exsolution lamellae as an oxidation process developed at temperatures above 600 °C.

Rojas (2017) identified a distinct chemical zonation in magnetite III, with a pronounced oscillatory pattern for Si and slightly for Al at the edge of magnetite crystals. These zonations were interpreted as a response to changing temperature and/or pH conditions of the hydrothermal fluid as it migrates to shallow depths.

**Event II** In samples from El Romeral, scapolite is a minor phase related to thin magnetite veinlets (magnetite type IV; Fig. 7). Two main possible origins have been proposed for this mineral phase: a regional-pneumatolytic origin generated by volatile contribution associated with magma crystallization or a secondary origin caused by the remobilization of host rock components during regional metamorphism (Sundius 1915; Mora and Vally 1989; Frietsch et al. 1997). The origin of scapolite alteration in the Norrbotten district, Sweden, has been attributed to metamorphism of evaporite layers. This early regional scapolite was later remobilized by hydrothermal fluids associated with the formation of IOCG deposits in this district (Frietsch et al. 1997; Bernal et al. 2017). At El Romeral, Na-rich scapolite (marialite) is a scarce alteration phase observed only in veinlets. Furthermore, no evaporite beds have been identified in the district; hence, we infer that halogens in scapolite may be sourced from fluids exsolved during the crystallization of arc magma, which commonly contains ≤ 3000 ppm Cl (Johnson et al. 2010), or from the andesite host rock (~ 130 ppm, Ewart 1982).

The scapolite event was followed by the crystallization of Ca-rich phases, where the assemblage epidote-calcite-titanite is observed in veinlets. This assemblage also supports a hydrothermal origin for this event with temperatures ranging between 200 and 350 °C (Reed 1997).

The presence of Ti phases, such as titanite and ilmenite surrounded by rutile, associated with magnetite II (Fig. 5c),

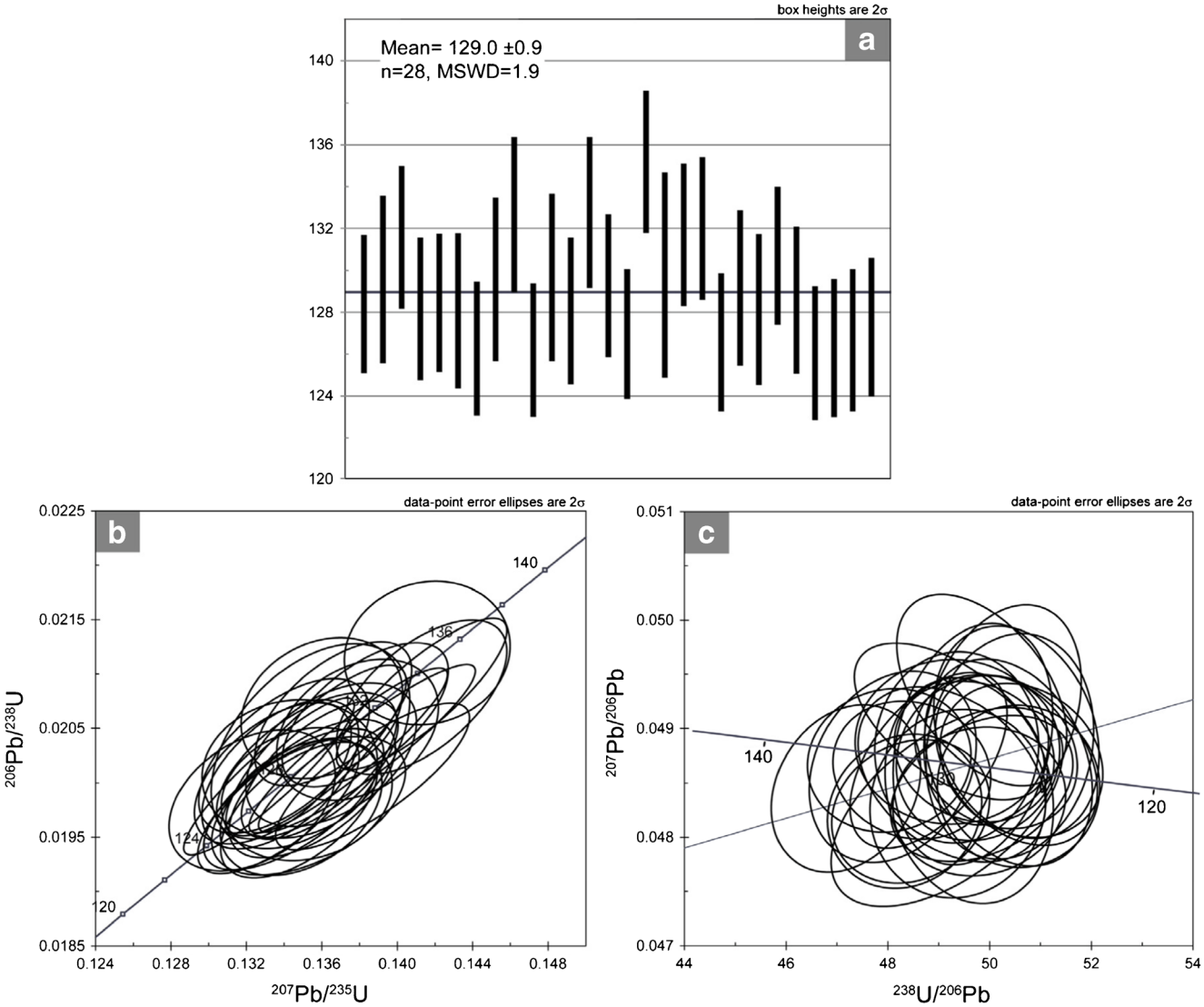


**Fig. 10** U-Pb ages for zircons from the Romeral diorite. **a** Weighted average. **b** Concordia diagram. **c** Tera-Wasserburg plot

plausibly reflects hydrothermal alteration (i.e., local dissolution-reprecipitation) of Ti-bearing magnetite that was deposited during the main mineralization event I. Similar observations have been reported for other IOA deposits (e.g., Pilot Knob and Pea Ridge, Missouri, USA; Day et al. 2016; Childress et al. 2016) and for porphyry-type ore deposits (e.g., El Teniente; Rabbia et al. 2009). Moreover, in porphyry copper deposits, rutile results from re-equilibration and/or breakdown of Ti-bearing minerals (e.g., biotite, Ti-magnetite, ilmenite), mainly at temperatures between 700 and 400 °C and in the presence of $SO_2$-rich oxidizing fluids (Williams and Cesbron 1977; Czamanske et al. 1981; Rabbia et al. 2009; Scott 2005). Titanium is compatible in the magnetite structure at high temperature but becomes increasingly incompatible with decreasing temperature (Nadoll et al. 2014). Titanium is generally immobile in hydrothermal fluids during weathering and low-grade metamorphism (Pearce and Cann 1973), but its solubility is enhanced by the formation of F and Cl complexes in acid solutions (Purtov and KoteVnikova 1993; Tanis et al. 2016). The presence of titanite, ilmenite, and rutile observed in samples from El Romeral supports a hydrothermal origin for these minerals.

Sulfide mineralization is characterized by the presence of pyrite with drop-shaped chalcopyrite and pyrrhotite (Fig. 6e). These equilibrium textures suggest precipitation from a hydrothermal fluid by abrupt cooling. The stability among these three mineral phases at 50 MPa (approximately 1.8 km depth) and 360 °C, reasonable T-P conditions for this sulfide event, reflects a sulfur fugacity (log $fS_2$) of ca. −9 and oxygen fugacity (log $fO_2$) less than −30 (Hezarkhani et al. 1999).

The final magnetite mineralization episode is represented by a restricted late event of disseminated magnetite (magnetite V) associated with secondary biotite (Fig. 5e). This late

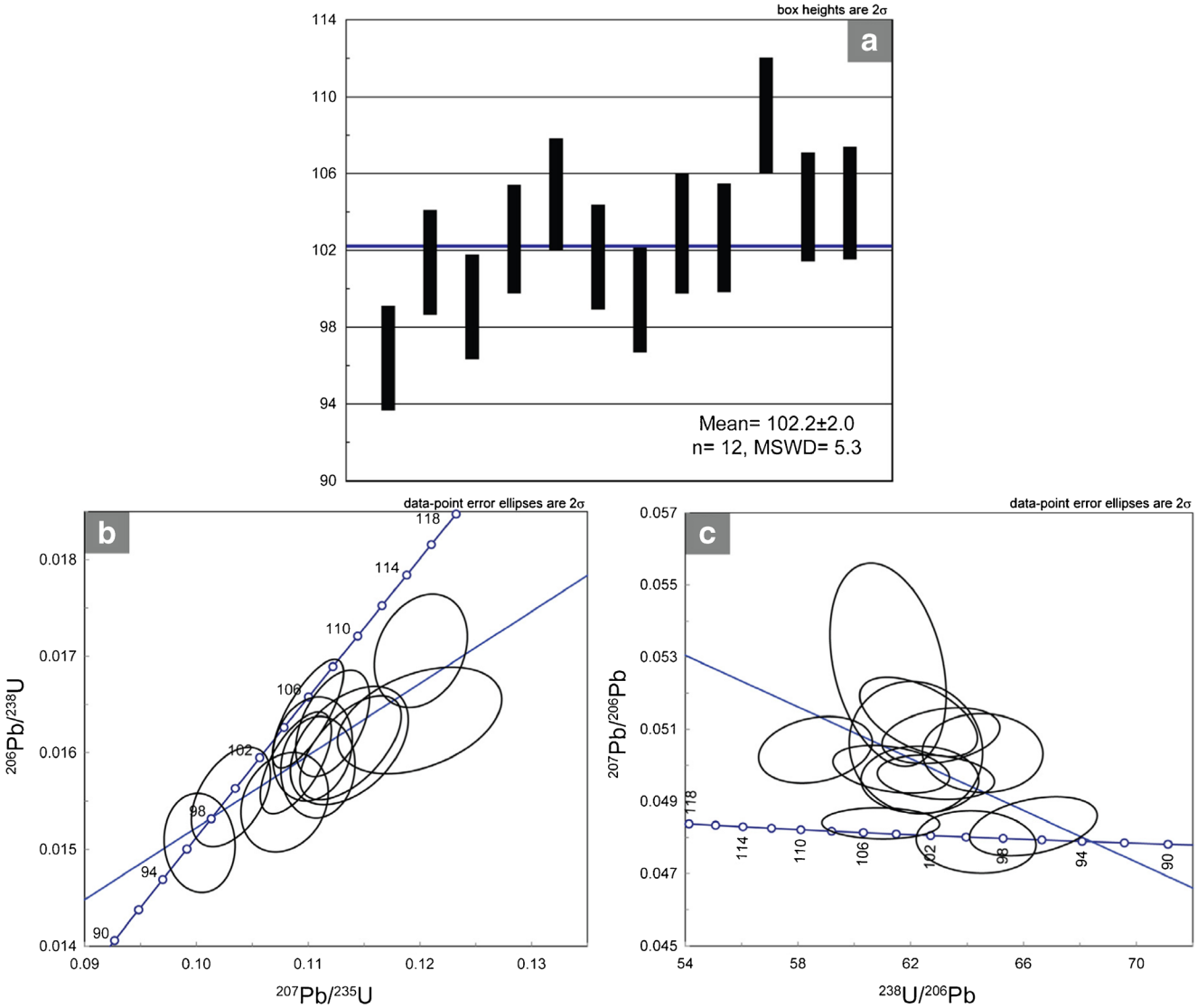


**Fig. 11** Punta de Piedra batholith U-Pb zircon ages. **a** Weighted average. **b** Concordia diagram. **c** Tera-Wasserburg plot

hydrothermal event is observed to have affected the host rocks in some areas around the magnetite ore body and is possibly related to the intrusion of post-ore dikes that resulted in potassic alteration. Potassic alteration in magmatic-hydrothermal systems, such as porphyry Cu deposits, has estimated formation temperatures between 550 and 650 °C (Seedorff et al. 2005; Sillitoe 2010).

Lastly, local hematite precipitation is described, related to minor chalcopyrite ± bornite that shows replacement by digenite/covellite in rims and fractures (Fig. 6f). This Cu enrichment follows a common reaction starting with bornite and ending with the crystallization of covellite, with intermediate digenite. These reactions reflect an increase in sulfur fugacity and progressively more acidic pH for the hydrothermal fluid (Barton 1970). Secondary Cu sulfides are evidence of a minor and restricted supergene event.

## Sulfur provenance using $\delta^{34}S$ signature

Sulfur isotope signatures for pyrite from El Romeral vary within a narrow range between − 0.8 and 2.9‰, with an average of ~ 0.7‰. These results indicate an exclusively magmatic sulfur contribution, i.e., without country rock assimilation or biogenic sulfur for the sulfide event. Delta-34 sulfur values for El Romeral sulfides are similar to those reported for other magnetite-apatite deposits from northern Chile (Fig. 12). However, some Chilean IOCG deposits (e.g., Mantoverde) do show a wider range of $\delta^{34}S$ values than reported here for El Romeral, indicating that the sulfur in some deposits may be sourced from more than one reservoir, including magmas and/or evaporites. It is worth mentioning that one measurement on a pyrite ± chalcopyrite sample yielded a higher value (2.9‰) than pure pyrite samples (ESM Table 4). Although a more detailed study on chalcopyrite must be performed to obtain

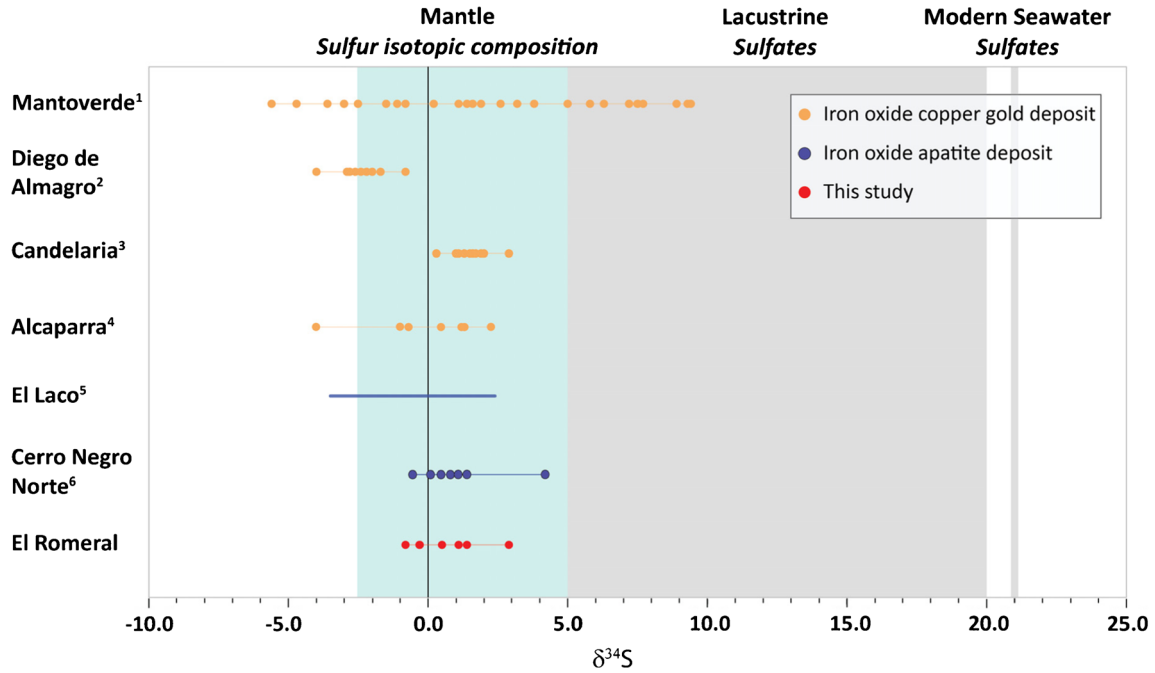


**Fig. 12** Diagram showing stable sulfur isotope values for IOCG and IOA deposits in the Chilean Iron Belt. Source of data: [1]Rieger et al. (2010); Loyola (2016); Marschik and Fontboté (2001); [4]Fredes (2017); [5]Henríquez (1991); [6]Salazar (2017)

more reliable conclusions, this variation in the isotope signature may reflect a different source for sulfur from the copper phase, or precipitation from a secondary fluid with different temperatures, redox conditions, or sulfur species (Vaughan and Craig 1978). One possible hypothesis calls upon the involvement of a fluid with a high oxygen fugacity or with heavier sulfur species, i.e., $H_2S$ (Vaughan and Craig 1978), which may have increased the isotope signature for this sample. Regardless, this value of 2.9‰ is still considered here as magmatic in origin (Fig. 12).

## Timing of mineralization and magmatism

The timing of the El Romeral formation was constrained by using U-Pb geochronology and $^{40}Ar/^{39}Ar$ thermochronology. The closure temperature for actinolite ranges between 550 and 650 °C (Dahl 1996; Villa et al. 1996), whereas for biotite, it is lower (ca. 450 °C; Villa and Puxeddu 1994). The Ar-degassing patterns (Figs. 8 and 9) for the dated samples do not show evidence of resetting; thus, the $^{40}Ar/^{39}Ar$ ages reported here can be considered robust. The U-Pb zircon crystallization age of 129.0 ± 0.9 Ma for the Romeral diorite (Fig. 10) is consistent with the $^{40}Ar/^{39}Ar$ ages (Fig. 8) for actinolite associated with the main magnetite ore formation. The temporal and spatial correspondence between the ore body and the Romeral diorite supports a genetic relationship between the mineralization and dioritic magmatism. Although a genetic relationship between diorite magmatism and the ore body has been previously suggested (Sillitoe 2003), these are the first geochronological data that support a direct link between magmatism and the magnetite ore for IOA deposits within the Chilean Iron Belt.

## Geodynamic model for the deposit formation

A new tectonic configuration was established in the area in Early Jurassic to late Early Cretaceous times associated with the onset of the Andean cycle. Renewed subduction with extensional conditions generated a rapidly subsiding arc at the current location of the Coastal Cordillera and a back-arc basin to the east of the arc coupled with the emplacement of large intrusive complexes (Coira et al. 1982; Brown et al. 1993; Scheuber 1994; Morata and Aguirre 2003). In the study area, the volcanic units are represented by the Early Jurassic to Early Cretaceous Agua Salada Subvolcanic Complex (Letelier 1977), whereas extensive magmatism is evidenced by several intrusive bodies emplaced during the initial transtensional tectonic conditions of the first substage of the Andean I period (late Early Jurassic to Kimmeridgian) (Fig. 13). This magmatic event is represented by pre-ore diorite intrusive bodies (ca. 145 Ma, Emparán and Pineda 2000) observed in the western section of the district (Fig. 2). Additionally, the Romeral diorite (~ 129 Ma) and the El Romeral iron ore (~128 Ma), along with the Cerro del Cobre pluton (~ 126 Ma; Emparán and Pineda 2000), were emplaced by the end of these extensional conditions and are related to the waning stages of this first substage (Fig. 13). Oyarzún et al. (2003) described this period as a transition to a transpressional regime south of Copiapó (Fig. 1), where overpressure induced magma ascent along the AFS, followed by IOA formation.

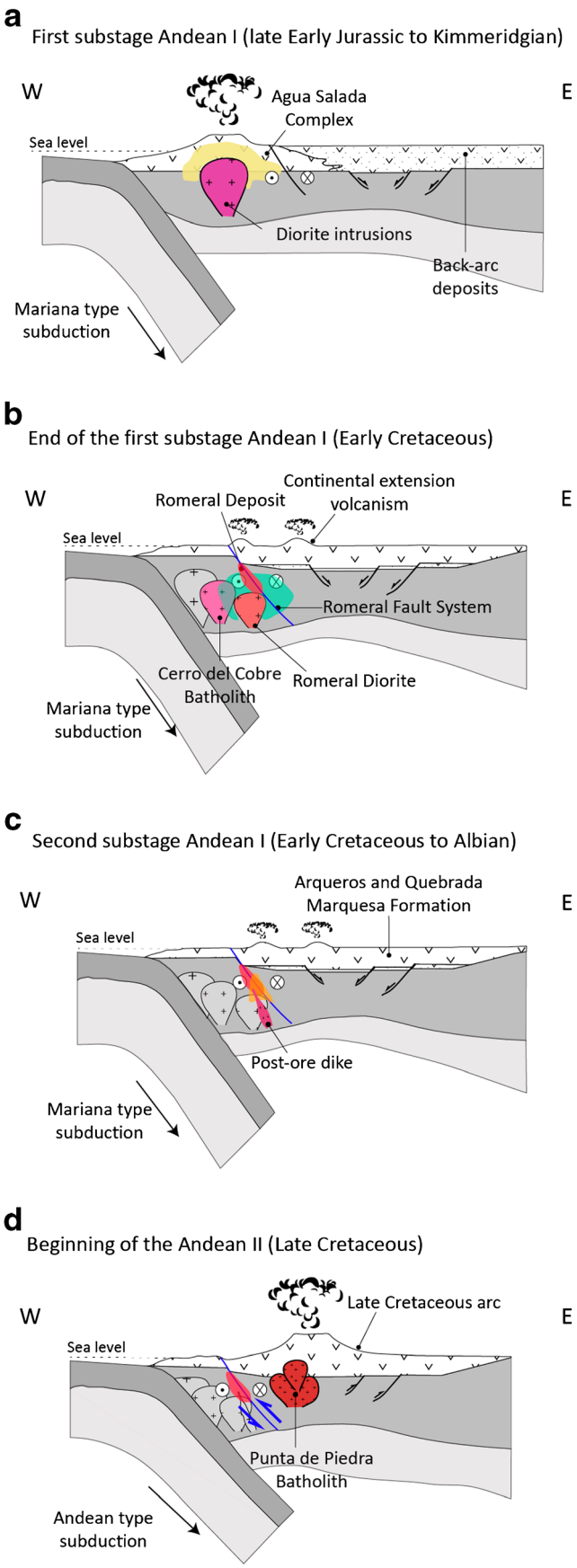


◀ **Fig. 13** Schematic east-west paleogeographic sections for the Andean I and the beginning of the Andean II (Peruvian Phase). Two main characteristic morphotectonic features are illustrated: a subsiding magmatic arc and transtensional structures (e.g., El Romeral Fault System). **a** Emplacement of diorite intrusions and development of pre-ore silicification (yellow halo around intrusions). **b** Intrusion of the Cerro del Cobre and the Romeral diorite with formation of the iron ore. The green halo represents pervasive actinolite and calcic alteration of the volcanic units. **c** Late hydrothermal magnetite with secondary biotite (orange) interpreted as formed by fluids exsolved from post-ore dikes. **d** Emplacement of the Punta de Piedra batholith during the beginning of the Andean II phase under a compressive regime. Note the change in fault displacement of the Romeral Fault System during the Late Cretaceous

During the second substage of the Andean I period (Kimmeridgian-Tithonian to Albian), a restricted magnetite mineralization event occurred at ~ 118 Ma, based on the hydrothermal biotite $^{40}Ar/^{39}Ar$ age reported here. This final mineralization event could be related to post-ore dikes (Fig. 13), which could supply Fe-rich fluids or remobilize primary magnetite resulting in a younger and restricted iron mineralization event.

At the end of the Andean I period, an episode of compressive Late Cretaceous deformation, the so-called "Peruvian Phase," inverted the former morphotectonic features, i.e., back-arc basin inversion and major fault systems (e.g., Atacama Fault System). This event is related to plate reorganization, causing northeastward displacement of the Farallon Plate and dextral oblique convergence, and to rapid ocean crust production and, therefore, to low-angle subduction (Charrier et al. 2007). In the La Serena area (Fig. 1), the Punta de Piedra granite to granodiorite batholith dated here at ~ 100 Ma (Fig. 11) is evidence of this episode (Fig. 13). This drastic change in the magma composition possibly reflects a different geotectonic regime, evidencing the beginning of the second Andean stage (late Early Cretaceous to Early Paleogene) that is characterized by a low-angle Andean-type subduction and a compressive tectonic regime (Fig. 13). This change in plate interactions marks the ending of IOA formation in the Coastal Cordillera of northern Chile (Fig. 13). Finally, the subduction of the Juan Fernandez Ridge resulted in a flat-slab zone with a high rate of uplift and erosion that exposed these ore deposits.

## Conclusions

El Romeral is one of the largest iron oxide-apatite (IOA) deposits in the Cretaceous Chilean Iron Belt. Textural observations of samples from El Romeral reveal five different types of magnetite: (i) an early inclusion-rich magnetite, which possibly corresponds to magmatic magnetite; (ii) an inclusion-poor magnetite associated with actinolite-clinopyroxene-quartz *pockets* and large actinolite crystals, interpreted to be related to a magmatic-hydrothermal process; (iii) an inclusion-poor zoned magnetite; (iv) hydrothermal magnetite with sulfides in veinlets that crosscut the massive ore body (composed mainly

by magnetite I and II crystals and minor magnetite III); and (v) a final and restricted hydrothermal event of disseminated magnetite with hydrothermal biotite aggregates in the host andesite. These five magnetite types represent a continuum from a magmatic to a magmatic-hydrothermal environment. Similar magnetite textures and late-stage hydrothermal magnetite-sulfide veinlets have also been described for the Los Colorados IOA deposits north of El Romeral (Knipping et al. 2015a, b; Reich et al. 2016).

Sulfur isotope data presented here ($\delta^{34}S$ between − 0.8 and 2.9‰), coupled with published $\delta^{34}S$ values for Andean IOA and IOCG deposits, support a hydrothermal origin for the sulfide mineralization (event II), with sulfur derived mainly from a magmatic source.

Uranium-Pb geochronology and $^{40}Ar/^{39}Ar$ thermochronology analysis provide four new ages for El Romeral that constrain the timing of magnetite formation at ca. 128 Ma. These new ages support a genetic link between the Romeral diorite and the Cerro Principal ore body. Both formed under extensional conditions during the waning stages of the first substage of the Andean I period, also known as Early Pacific stage (135–120 Ma) (Chen et al. 2013). The late minor hydrothermal magnetite mineralization associated with potassic (biotite) alteration occurred at ~ 118 Ma and was caused by Fe remobilization related to the intrusion of post-ore dikes during the beginning of the second substage of the Andean I period (i.e., Late Pacific stage, 120–100 Ma; Chen et al. 2013). On a regional scale, this period is characterized by a compressive regime that led to basin inversion and major formation of IOCG deposits in central-southern Peru and northern Chile (Chen et al. 2013). The emplacement of the Punta de Piedra batholith (~ 100 Ma) marked the beginning of the Andean II stage and the end of Kiruna-type deposit formation in the area.

Although more investigations are needed to confirm a temporal and genetic link between widespread iron mineralization and synchronous intermediate-composition magmatism leading to the formation of the Chilean Iron Belt, our data from El Romeral point to a predominant role for dioritic magmas in the formation of iron oxide-apatite mineralization, which agrees with studies performed at the Los Colorados IOA deposit within the same belt (Knipping et al. 2015a, b; Bilenker et al. 2016; Reich et al. 2016).

**Acknowledgements** We acknowledge the reviewers Patrick Williams and Daniel Harlov for their constructive comments that greatly improve the manuscript. Bernd Lehmann is thanked for the editorial handling and for additional comments on the manuscript. We acknowledge the facilities and technical assistance of the Isotopic Geology Unit at the SERNAGEOMIN Laboratory Centre for Ar/Ar dating and Mathieu Leisen from CEGA for U-Pb dating. David Dettmann from the University of Arizona, Tucson, is thanked for the sulfur isotope analyses.

**Funding information** This study was funded by FONDECYT grant no. 1140780 to FB. We thank for the additional support from the Millennium Science Initiative (MSI) through Millennium Nucleus for Metal Tracing along Subduction grant NC130065, and the Servicio Nacional de Geología y Minería (SERNAGEOMIN). We appreciate the support and help from the geology team at Compañía Minera del Pacífico (CMP).

## References

Alva-Valdivia LM, Rivas-Sánchez ML, Goguitchaichvili A, Urrutia-Fucugauchi J, Gonzalez A, Vivallo W (2003) Integrated magnetic studies of the El Romeral iron-ore deposit, Chile: implications for ore genesis and modeling of magnetic anomalies. J Appl Geophys 53:137–151

Barra F, Reich M, Selby D, Rojas P, Simon A, Salazar E, Palma G (2017) Unraveling the origin of the Andean IOCG clan: a Re-Os isotope approach. Ore Geol Rev 81:62–78

Barton PB (1970) Sulfide Petrology. Mineral Soc Am Spec Pap 3:187–198

Bernal NF, Gleeson SA, Smith MP, Barnes JD, Pan Y (2017) Evidence of multiple halogen sources in scapolites from iron oxide-copper-gold (IOCG) deposits and regional Na Cl metasomatic alteration, Norrbotten County, Sweden. Chem Geol 451:90–103

Bilenker LD, Simon AC, Reich M, Lundstrom CC, Gajos N, Bindeman I, Barra F, Munizaga R (2016) Fe-O stable isotope pairs elucidate a high-temperature origin of Chilean iron oxide-apatite deposits. Geochim Cosmochim Acta 177:94–104

Black LP, Kamo SL, Allen CM, Davis DW, Aleinikoff JN, Valley JW, Mundil R, Campbell IH, Korsch RJ, Williams IS, Foudoulis C (2004) Improved Pb-206/U-218 microprobe geochronology by the monitoring of a trace-element-related matrix effect; SHRIMP, ID-TIMS, ELA-ICP-MS and oxygen isotope documentation for a series of zircon standards. Chem Geol 205:115–140

Bookstrom A (1975) Magnetite deposits of El Romeral, Chile: physical geology, sequence of events, and processes of formation. PhD Dissertation, Stanford University, 417 p

Bookstrom A (1977) The magnetite deposits of El Romeral, Chile. Econ Geol 72:1101–1130

Brown M, Díaz F, Grocott J (1993) Displacement history of the Atacama Fault System, 25°00′S 27°00′S, northern Chile. Geol Soc Am Bull 105:1165–1174

Buddington AF, Lindsley DH (1964) Iron-titanium oxide minerals and synthetic equivalents. J Petrol 5:310–357

Charrier R, Pinto L, Rodríguez MP (2007) Tectonostratigraphic evolution of the Andean Orogen in Chile. In: Moreno T, Gibbons W (eds) The geology of Chile. Geological Society, London, pp 21–114

Chen H, Clark AH, Kyser K, Ullrich TD, Baxter R, Chen Y, Moody TC (2010) Evolution of the giant Marcona-Mina Justa iron oxide-copper-gold district, South-Central Peru. Econ Geol 105:155–185

Chen H, Cooke DR, Baker MJ (2013) Mesozoic iron oxide copper-gold mineralization in the Central Andes and the Gondwana supercontinent breakup. Econ Geol 108:37–44

Childress TM, Simon AC, Day WC, Lundstrom CC, Bindeman IN (2016) Iron and oxygen isotope signatures of the pea ridge and pilot knob magnetite–apatite deposits, southeast Missouri, USA. Econ Geol 111:2033–2044

Coira B, Davidson C, Mpodozis C, Ramos V (1982) Tectonic and magmatic evolution of the Andes of nothern Argentina and Chile. Earth Sci Rev 18:303–332

Coleman ML, Moore MP (1978) Direct reduction of sulfates to sulfur dioxide for isotopic analysis. Anal Chem 50:1594–1598

Corfu F, Hanchar JM, Hoskin PWO, Kinny P (2003) Atlas of zircon textures. Rev Miner Geochem 53:469–500

Czamanske GK, Force ER, Moore WJ (1981) Some geologic and potential resource aspects of rutile in porphyry copper deposits. Econ Geol 76:2240–2246

Dahl PS (1996) The effects of composition on retentivity of Ar and O in hornblende and related amphiboles: a field-tested empirical model. Geochim Cosmochim Acta 60:3687–3700

Day WC, Slack JF, Ayuso RA, Seeger CM (2016) Regional geologic and petrologic framework for iron oxide ± apatite ± rare earth element and iron oxide copper-gold deposits of the Mesoproterozoic St. Francois Mountains terrane, southeast Missouri, USA. Econ Geol 111:1825–1858

Edmonds M, Mather TA (2017) Volcanic sulfides and outgassing. Elements 13:105–110

Emparan C, Pineda G (2000) Area La Serena-La Higuera, Región de Coquimbo. Servicio Nacional de Geología y Minería. Mapas Geológicos, no.18, 1 mapa escala 1:100.000, Santiago

Emparan C, Pineda G (2005) Geología del Área Andacollo-Puerto Aldea, Región de Coquimbo. Servicio Nacional de Geología y Minería. Carta Geológica de Chile, Serie Geología Básica, no. 96, 1: 1000.000, Santiago

Espinoza L (2000) Estudio petrográfico del cuerpo Cerro Principal del distrito ferrífero El Romeral IV región- La Serena, Chile. Honors thesis, Universidad de Chile, Santiago, Chile

Ewart A (1982) The mineralogy and petrology of tertiary-recent orogenic volcanic rocks: with special reference to the andesitic-basaltic compositional range. In: Thorpe RS (ed) Andesites, orogenic andesites, and related rocks. Wiley, New York, pp 26–95

Fredes MJ (2017) Geología del prospecto IOCG Alcaparra, Comuna de Huasco, Región de Atacama. Honors thesis, Universidad de Chile, Santiago, Chile

Frietsch R, Tuisku P, Martinsson O, Perdahl J (1997) Early Proterozoic Cu-(Au) and Fe ore deposits associated with regional Na-Cl metasomatism in northern Fennoscandia. Ore Geol Rev 12:1–34

Frutos J, Oyarzún J (1975) Tectonic and geochemical evidence concerning the genesis of El Laco magnetite lava flow deposits, Chile. Econ Geol 70:988–990

Henríquez F (1991) Internal report FONDECYT 89-0759. CONICYT, Santiago

Hezarkhani A, Williams-Jones AE, Gammons CH (1999) Factors controlling copper solubility and chalcopyrite deposition in the Sungun porphyry copper deposit, Iran. Mineral Deposita 34:770–783

Jaillard E, Soler P, Carlier G, Mourier T (1990) Geodynamic evolution of the northern and central Andes during early to middle Mesozoic times: a Tethyan model. J Geol Soc 147:1009–1022

Johnson ER, Wallace PJ, Cashman KV, Granados HD (2010) Degassing of volatiles ($H_2O$, $CO_2$, S, Cl) during ascent, crystallization and eruption at mafic monogenetic volcanoes in Central Mexico. J Volcanol Geotherm Res 197:225–238

Jugo PJ, Candela PA, Piccoli PM (1999) Magmatic sulfides and Au/Cu ratios in porphyry deposits: an experimental study of copper and gold partitioning at 850°C, 100 MPa in haplogranitic melt-pyrrhotite-intermediate solid solution-gold metal assemblage, at gas saturation. Lithos 46:573–589

Knipping JL, Bilenker LD, Simon AC, Reich M, Barra F, Deditius AP, Lundstrom C, Bindeman I, Munizaga R (2015a) Giant Kiruna-type deposits form by efficient flotation of magmatic magnetite suspensions. Geology 43:591–594

Knipping JL, Bilenker LD, Simon AC, Reich M, Barra F, Deditius AP, Wälle M, Heinrich CA, Holtz F, Munizaga R (2015b) Trace elements in magnetite from massive iron oxide-apatite deposits indicate a combined formation by igneous and magmatic-hydrothermal processes. Geochim Cosmochim Acta 171:15–38

Koppers AAP (2002) ArArCALC-software for $^{40}Ar/^{39}Ar$ age calculations. Comput Geosci 28:605–619

Kullerud G, Yoder HS (1959) Pyrite stability relations in the Fe-S system. Econ Geol 54:533–572

Letelier M (1977) Petrología y ambiente de depositación y estructura de las Formaciones matahuaico, Las Breas, Tres Cruces sensu lato e intrusivos permotriásicos en el área de Rivadavia-Alcohuás, valle de Elqui, IV Región, Chile. Honors thesis, Universidad de Chile, Santiago, Chile

Loyola N (2016) Origen de la mineralización y alteración hidrotermal del depósito tipo IOCG Diego de Almagro, III Región de Atacama, Chile. Honors thesis, Universidad de Chile, Santiago, Chile, 41–42

Ludwig K (2010) Isoplot/Ex version 4.1, a geochronological toolkit for Microsoft Excel: Berkeley Geochronology Center, Spec Publ 4

Maksaev V (1990) Metallogeny, geological evolution and thermochronology of the Chilean Andean between latitudes 21° and 26° south, and the origin of the major porphyry copper deposits. PhD Dissertation, Dalhousie University, Halifax, Nova Scotia, Canada

Marschik R, Fontboté L (2001) The Candelaria-Punta del Cobre iron oxide Cu-Au(-Zn-Ag) deposits, Chile. Econ Geol 96:1799–1826

Ménard JJ (1995) Relationship between altered pyroxene diorite and the magnetite mineralization in the Chilean Iron Belt, with emphasis on the El Algarrobo iron deposits (Atacama region, Chile). Mineral Deposita 30:268–274

Mora CI, Vally JW (1989) Halogen-rich scapolite and biotite: implications for metamorphic fluid-rock interaction. Am Mineral 74:721–737

Morata D, Aguirre L (2003) Extensional Lower Cretaceous volcanism in the coastal range (29°20′-30°S), Chile: geochemistry and petrogenesis. J S Am Earth Sci 16:459–476

Nadoll P, Angerer T, Mauk JL, French D, Walshe J (2014) The chemistry of hydrothermal magnetite: a review. Ore Geol Rev 61:1–32

Naslund HR, Henríquez F, Nyström JO, Vivallo W, Dobbs FM (2002) Magmatic iron ores and associated mineralisation examples from the Chilean high Andes and Coastal Cordillera. In: Porter TM (ed) Hydrothermal iron oxide copper-gold & related deposits: a global perspective, vol 2. PGC, Adelaide, pp 207–226

Nyström JO, Henríquez F (1994) Magmatic features of iron ores of the Kiruna type in chile and ore textures and magnetite geochemistry. Econ Geol 89:820–839

Oyarzún R, Oyarzún J, Ménard JJ, Lillo J (2003) The Cretaceous iron belt of northern Chile: role of oceanic plates, a superplume event, and a major shear zone. Mineral Deposita 38:640–646

Pankratz LB, King EG (1970) High-temperature enthalpies and entropies of chalcopyrite and bornite. US Bureau of Mines. Rep Investig 7435:1–10

Parak T (1975) Kiruna iron ores are not "intrusive-magmatic ores of the Kiruna type". Econ Geol 70:1242–1258

Paton C, Hellstrom J, Paul B, Woodhead J, Hergt J (2011) Iolite: freeware for the visualization and processing of mass spectrometric data. J Anal At Spectrom 26:2508–2518

Pearce JA, Cann JR (1973) Tectonic setting of basic volcanic rocks determined using trace element analyses. Earth Planet Sci Lett 19:290–300

Purtov VK, KoteVnikova AL (1993) Solubility of titanium in chloride and fluoride hydrothermal solutions. Int Geol Rev 35:279–287

Rabbia OM, Hernández LB, French DH, King RW, Ayers JC (2009) The El Teniente porphyry Cu-Mo deposit from a hydrothermal rutile perspective. Mineral Deposita 44:849–866

Reed M (1997) Hydrothermal alteration and its relationship to ore fluid composition. In: Barnes HL (ed) Geochemistry of hydrothermal ore deposits, 3rd edn. Wiley, New York, pp 303–365

Reich M, Simon AC, Deditius A, Barra F, Chryssoulis S, Lagas G, Tardani D, Knipping J, Bilenker L, Sánchez-Alfaro P, Roberts MP, Munizaga R (2016) Trace element signature of pyrite from the Los Colorados iron oxide-apatite (IOA) deposit, Chile: a missing link between Andean IOA and iron oxide copper-gold systems? Econ Geol 111:743–761

Rhodes AL, Oreskes N, Sheets S (1999) Geology and rare earth element geochemistry of magnetite deposits at El Laco, Chile. In: Brian JS (ed) Geology and ore deposits of the Central Andes. SEG Spec Publ 7, pp 299–332

Rieger AA, Marschik R, Díaz M, Hölzl S, Charadia M, Akker B, Spangenberg JE (2010) The hypogene iron oxide copper-gold mineralization in the Mantoverde district, northern Chile. Econ Geol 105:1271–1299

Rojas PA (2017) Genesis of the El Romeral iron ore: new contributions to the understanding of iron oxide-apatite deposits. MSc thesis, Universidad de Chile, Santiago, Chile, pp 160

Salazar E (2017) Geoquímica de magnetitas como indicador petrogenético del depósito Cerro Negro Norte, Copiapó, Chile. MSc thesis, Universidad de Chile, Santiago, Chile

Scheuber E (1994) Tektonische Entwicklung des nordchilenischen aktiven Kontinentalrandes: Der Einfluss von Plattenkonvergenz und Rheologie. Geoteckt Forsch 81:1–131

Scheuber E, Andriessen PAM (1990) The kinematic and geodynamic significance of the Atacama fault zone, northern Chile. J Struct Geol 12:243–257

Scott KM (2005) Rutile geochemistry as a guide to porphyry Cu-Au mineralization, Northparkes, New South Wales, Australia. Geochem Explor Environ Anal 5:247–253

Seedorff E, Dilles JH, Proffett Jr JM, Einaudi MT, Zurcher L, Stavast WJA, Johnson DA, Baton MD (2005) Porphyry deposits: characteristics and origin of hypogene features. In: Econ Geol 100th Anniv Vol, p. 251–298

Sillitoe RH (2003) Iron oxide-copper-gold deposits: an Andean view. Mineral Deposita 38:787–812

Sillitoe RH (2010) Porphyry copper systems. Econ Geol 105:3–41

Sillitoe RH, Burrows DR (2002) New field evidence bearing on the origin of the El Laco magnetite deposit, northern Chile. Econ Geol 97: 1101–1109

Sláma J, Košler J, Condon D, Crowley J, Gerdes A, Hanchar J, Horstwood M, Morris G, Nasdala L, Norberg N, Schaltegger U, Schoene B, Tubrett M, Whitehouse M (2008) Plešovice zircon: a new natural reference material for U–Pb and Hf isotopic microanalysis. Chem Geol 249:1–35

Sundius N (1915) Beiträge zur Geologie des siidlichen Teils des Kirunagebiets. Vetensk Prakt Unders Lappl, pp 1–237

Tanis EA, Simon AC, Zhang Y, Chow P, Xiao Y, Hanchar JM, Tschauner O, Shen G (2016) Rutile solubility in NaF-NaCl-KCl-bearing aqueous fluids at 0.5-2.79 GPa and 250-650°C. Geochim Cosmochim Acta 177:170–181

Vaughan DJ, Craig JR (1978) Mineral chemistry of metal sulfides. Cambridge University Press, Cambridge

Villa IM, Puxeddu M (1994) Geochronology of the Larderello geothermal field: new data and the 'closure temperature' issue. Contrib Miner Petrol 115:415–426

Villa IM, Grobéty B, Kelley SP, Trigila R, Wieler R (1996) Assessing Ar transport paths and mechanisms for McClure Mountains hornblende. Contrib Miner Petrol 126:67–80

Williams S, Cesbron F (1977) Rutile and apatite: useful prospecting guides for porphyry copper deposits. Mineral Mag 41:288–292